Prediction of dehydration performance of supersonic separator based on a multi-fluid model with heterogeneous condensation

Hongbing Ding[1], Chunqian Sun[1], Chao Wang[1, *], Chuang Wen[2], Yuhe Tian[1]

[1]Tianjin Key Laboratory of Process Measurement and Control, School of Electrical and Information Engineering, Tianjin University, Tianjin 300072, China

[2]Faculty of Engineering, University of Nottingham, University Park, Nottingham NG7 2RD, UK

*Corresponding author: Chao Wang, Email: wangchao@tju.edu.cn

Abstract: Supersonic separation is a novel technology. A multi-fluid slip model for swirling flow with homogenous/heterogenous condensation and evaporation processes in the supersonic separator was built to estimate the separation efficiency. This model solves the governing equations of compressible turbulent gas phase and dispersed homogenous/heterogenous liquid phase considering droplet coalescence and interphase force. Its prediction accuracy for condensation and swirling flows was validated. Then, the flow field, slip velocity and droplet trajectory inside the separators with different swirl strengths were investigated. The maximum values of radial slip velocity are 29.2 and 8.26 m/s for inlet foreign droplet radius of 1.0 and 0.4 micron. It means the larger foreign droplet has a better condensation rate. However, the residence time of larger foreign droplet in core flow is shorten. Thus, the inlet radius of foreign droplet has to be moderate for best separation efficiency. Finally, the dehydration performances of separator were evaluated. The optimal radius of inlet foreign droplet to maximize the dehumidification and efficiency was found. For the separator with swirl strength of 22%, the optimal radius is 0.85 micron at inlet pressure of 250 kPa, where the maximum dew point depression is 42.41 °C and the water removal rate is 87.82%.

Keywords: Supersonic separator; Condensation and evaporation; Multi-fluid model; Natural gas dehydration; Separation efficiency

Nomenclature

A	area, m^2	x_a, x_r	axial and radial coordinates, m
a_k	heat transfer coefficient, W m^{-2} K^{-1}	Y_k, Y_ω	the dissipations of k and ω
C_c	Cunningham slip correction factor, -	*Greek*	
c	sound speed, m s^{-1}	α	volume fraction, -
c_p	specific heat capacity, J kg^{-1} K^{-1}	β	gas-liquid mass ratio, -
c_s	species mass fraction, -	Γ	specific heat ratio, -
D_s	Mass diffusion coefficient, m^2 s^{-1}	γ	pressure loss ratio, -
D_T	subcooling, °C	ΔT	dew point depression, °C
D_ω	cross-diffusion term, kg m^{-3} s^{-2}	δ_{ij}	Kronecker delta, -

d	throat diameter of nozzle, mm	η	water removal rate, %
E	total energy, J kg^{-1}	λ	thermal conductivity, W m^{-1} K^{-1}
F_D	drag force, kg m^{-2} s^{-2}	μ	dynamic viscosity of fluid, Pa s
f	collision frequency, Hz	ρ	density of fluid, kg m^{-3}
G_k, G_ω	the generations of k and ω	σ	surface tension, N m^{-1}
h_{lg}	latent heat of water vapor, J kg^{-1}	σ_k, σ_ω	turbulent Prandtl numbers, -
J	homogeneous nucleation rate, m^{-3} s^{-1}	τ_{ij}	deviatoric stress tensor, Pa
K	bulk elastic modulus, Pa	υ	single water molecule volume, m^3
Kn	Knudsen number, -	Φ	relative humidity, $p_v/p_s(T_g)\times 100$ %
k	turbulence kinetic energy, J kg^{-1}	χ	mole fraction of water vapor, -
k_B	Boltzmann's constant. 1.38×10^{-23} J K^{-1}	ψ	recovery of dry gas at the outlet
M	dimensionless mass flow rate, -	Ω	magnitude of strain rate, s^{-1}
Ma	Mach number, -	ω	specific dissipation rate, s^{-1}
m_m	mass of water molecule, 2.99×10^{-26} kg	*Subscripts*	
m	liquid mass changing rate, kg m^{-3} s^{-1}	*	stagnation condition
n	droplet number concentration, m^{-3}	a, r, t	axial, radial, tangential
Pr	Prandtl number, -	c	critical
p	pressure, Pa	d	dew point
Q	mass flow-rate, kg s^{-1}	eff	effective
Re_p	Reynolds number	g	gas
R_g	gas constant of air, J $kg^{-1}\cdot K^{-1}$	het	heterogeneous
R_v	specific gas constant of water vapor, J $kg^{-1}\cdot K^{-1}$	hom	homogeneous
r	droplet radius, m	i, j, k	tensor notation
S	swirl strength, -	k	species
S_s	supersaturation of water vapor, -	l	liquid
$S_{i,j}$	mean strain rate, s^{-1}	rel	relative
T	fluid temperature, °C	s	saturation
T_R	reduced temperature, -	tu	turbulent
T_r	droplet surface temperature, °C	v	water vapor
t	time, s	*Superscripts*	
u	velocity of fluid, m s^{-1}	in, out	Inlet, outlet
Vs	interphase slip velocity, m s^{-1}	nt	nozzle throat
x_j	Cartesian coordinates (tensors), m	dry, wet	dry and wet gas outlets

1. Introduction

Natural gas as a popular and cleaner alternative to coal and other fossil fuel, plays a crucial role in the next decades and reduces the carbon and other emissions leading to the long-term benefits for public health and the environment [1]. However, the presence of water vapor, heavy hydrocarbons and carbon dioxide (CO_2) [2] in raw natural gas causes several problems, such as reduction of heating value [3], corrosion of water combined with the sour gases including CO_2 and H_2S, formation of hydrate, the blockage of equipment and pipelines, and CO_2 emission [4]. Therefore, separation technology is crucial for natural gas processing [5]. Several separation techniques can be utilized for the natural gas processing, including adsorption, absorption, cryogenic separation, turbine expansion, and Membranes [6]. However, these technologies have some disadvantages, such as complex structure, large equipment, huge investment and possibility of environmental pollution.

The supersonic separator operated without rotating parts and chemicals is a revolutionary technique for removing water vapor and heavy hydrocarbons from natural gas [7]. It also potentially uses for CO_2 removal in CCS (carbon capture and storage). As a simple, reliable and environmentally friendly separator [8], the condensable vapor is condensed instantaneously during the gas expansion, and then separated from the natural gas because of the strong centrifugal force [9]. It can prevent the hydrate problem without any inhibitor and regeneration system because of the low temperature and short residence time inside the supersonic separator [10]. Although many works have been done for optimizing the structure and performance of supersonic separator, the actual dehydration performance is still far from being satisfactory, as the flow inside supersonic separator is quite complex which includes condensation, evaporation, vorticity, turbulence, shockwave and interphase slip.

The goal of supersonic separator is to remove condensable vapors from the gas flow and achieve a lower dew point or strip the gas of heavy hydrocarbons. The dew point depression and water removal rate of the supersonic separator are really desired. Currently, there are two approaches for predicting its separation performance, the computational fluid dynamics using Fluent software [4] and the process simulation conducted in Aspen HYSYS [11].

For process simulation, Karimi and Abdi [12] investigated the flow field of single-phase gas in a Laval nozzle without swirl by using Aspen HYSYS, and found the gas could potentially be dehydrated to very low water dew point. Wen et al. [13] compared the temperature and pressure profiles obtained by FLUENT with phase envelope diagrams by HYSYS and found the supersonic separators is suitable for liquefied natural gas. Hammer et al. [14] investigated CO2 removal of supersonic separator from dry 2.98% CO2 exhausts by using Aspen HYSYS. Niknam et al. [15] used Aspen HYSYS to predict the 3S unit performance by conventional unit operations, then analyzed the performance of nozzle and proposed an efficiency model for supersonic separation by integrating COMSOL, HYSYS and MATLAB software [16]. Arinelli et al. [17] developed two steady state Unit Operation Extensions (UOE) and the vapor-liquid equilibrium (VLE) envelopes for HYSYS 8.8 to simulate supersonic separator and membrane permeation for treating humid natural gas with 44%mol CO2. Bian et al. [18] proposed a novel gas liquefaction process and the liquefaction efficiency under different condition were calculated by using

MATLAB and HYSYS. Rezakazemi et al. [19] carry out a series of process simulation by Aspen HYSYS to compare recovery of ethane from typical JT Valve, Turbo-Expander and Twister Technology . Brigagão et al. [20] developed a new CCS unit by using a supersonic separator based on HYSYS 8.8. CO2 emissions can be reduced by 43% with economic performance. de Medeiros et. al [21]-[22] proposed UOE module for estimating sound speed of two-phase systems in supersonic reactors for multiphase multi-reactive equilibrium system via HYSYS. However, it is recognized that their results were not validated against experimental data.

For CFD simulation, Malyshkina [23] numerically investigated the single-phase swirling flow inside a supersonic separator and analyzed effects of Mach number and temperature on recovery of pressure. Wen et al. [24]-[25] studied the flow characteristics and mass flux inside a supersonic separator with and without swirls. Wang and Hu [26] investigate the effects of swirling generator and drainage structure where the RNG k-ε turbulence model was utilized. Liu [27] established a three-dimensional single-phase numerical model considering the compressible and strong swirling effect to study the flow field and to optimize separation performance. Alnoush and Castier [28] proposed a shortcut one-dimensional single-phase numerical modeling for the conceptual preliminary design of supersonic separator.

On this basis, two-phase models based on the discrete particle method (DPM) were built. Wen et al. [29] and Yang et al. [30] studied natural gas flow characteristics and particle separation behavior by using DPM model with particle diameter constant of 1.4 micron. Liu et al. [31] also predicted the particle behavior inside a supersonic separator employing the DPM model, where the particle diameter range is from 10 to 50 micron, However, the typical particle size in the supersonic separator is 0.1-2 micron [32] from Twister BV. Jiang [33] studied the gas flow field and CO_2 droplet trajectory inside a supersonic separator employing DPM model. The size of CO_2 droplet is set to be a constant of 1.25 micron. However, these researches do not consider the complex nucleation-condensation process of condensable vapor and the evaporation process of droplet inside the supersonic separator.

Take into account the condensation process in the supersonic flow, Ma et al. [34] built an Eulerian two-fluid model to investigate homogenous condensing flow in a Laval nozzle. Shooshtari and Shahsavand [35] provided a new theoretical approach based on mass transfer rate to predict liquid droplet growth of homogenous condensation of binary mixtures in a Laval nozzle. Ding et al. [36] proposed an analytical solution to predict Wilson point of homogeneous nucleation inside the nozzle. Castier [37] conducted several numerical simulations for the natural gas partial condensation inside a Laval nozzle without swirl. Dykas [38]-[39] built an in-house CFD code with 3-D RANS equations for single-fluid no-slip model to predict the wet steam and moist air condensation process within a Laval nozzle. Wen et al. [4] developed a numerical model of homogenous nucleation to predict CO_2 condensation because of condensation inside supersonic flows. The condensation model predicted 18.6% of condensed liquid fraction.

Actually, raw natural gas usually contains foreign droplets before entering into the supersonic separator in practical operation and laboratory tests, and leads to the heterogeneous condensation. This process can effectively reduce the free energy barrier and promotes the condensation appearance. Ma et al. [40] experimentally investigated the effect of foreign droplets on vapor condensation by using droplet

enlargement according to heterogeneous condensation theory. Ding et al. [41] carried out a two-dimensional multi-phase turbulence model for homogeneous/heterogeneous condensation to investigate the effect of condensation on mass flow rate of Laval nozzle without swirl. Niknam et al. [42] experimentally obtained dehydration of low-pressure gas in supersonic separator with heterogeneous condensation of water droplets containing small foreign droplet and built a two-phase Euler-Euler model in 2D asymmetric domain for analyzing the dehydration efficiency. However, they did not consider homogenous nucleation process and the drag model was not provided. Shooshtari and Shahsavand [43] built a heterogeneous condensation model without interphase slip for optimizing geometry of the Laval nozzle which was validated by Dykas's predictions [44]. Bian et al. [45] built a physical model for homogenous and heterogeneous condensations in a Laval nozzle. However, the interphase slip velocity was ignored which is not suitable for the swirling flow in a supersonic separator.

As mentioned above, there is a lack of CFD model for accurate prediction of liquid droplets trajectories inside supersonic separator with combination of swirling, nucleation, growth, evaporation, slip, collision and coalescence in respect of the operation optimization of the supersonic separator. This paper proposed a novel multi-fluid (slip) model for the swirling flow with the homogenous/heterogenous condensation and evaporation processes in supersonic separator. The mathematical modeling and performance assessment of present multi-fluid model have been conducted. It provides an effective method to analyze the effects of homogeneous/heterogeneous condensation with enhanced heat transfer coefficient due to strong swirl on the dehydration efficiency of supersonic separator.

2. Supersonic separator

In this paper, the supersonic separator is composed of a central body and some vanes were designed, as shown in Fig. 1. The annular channel between the central inner body and the shell wall forms a supersonic nozzle section, a cyclonic separation section and a diffuser with the dry and wet gas outlets [24]. The swirling flow is generated by several static vanes with specific turning angle at the subsonic section which can control the flow swirl strength.

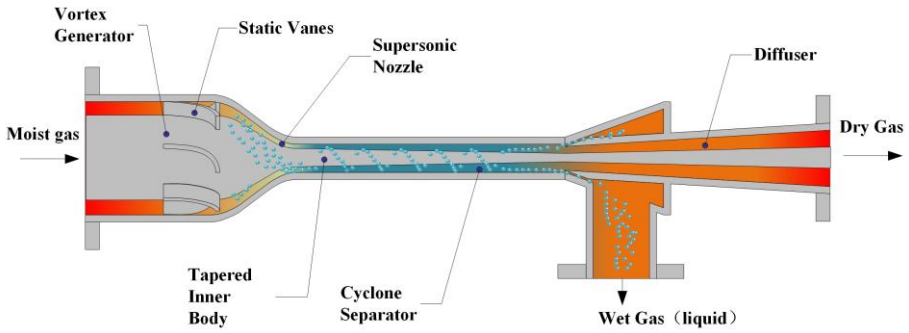

Fig. 1. Structural diagram of supersonic separator with a swirling generator.

Several parameters related to the separation efficiency and hydration performance were defined. The pressure loss ratio γ is expressed as

$$\gamma = \frac{p^{\text{in}} - p^{\text{out}}}{p^{\text{in}}} \tag{1}$$

where p is the pressure of the fluid. The superscripts in and out represent inlet and outlet conditions.

The recovery of dry gas at the outlet is defined as

$$\psi = \frac{Q^{\text{dry}}}{Q^{\text{in}}} \times 100\% = \frac{Q^{\text{in}} - Q^{\text{wet}}}{Q^{\text{in}}} \times 100\% \tag{2}$$

where Q^{in} , Q^{dry} and Q^{wet} represent the mass flow rates at inlet, dry and wet gas outlets.

The dew point depression ΔT_{d} is defined as [40],

$$\Delta T_{\text{d}} = T_{\text{d}}^{\text{in}} - T_{\text{d}}^{\text{out}} \tag{3}$$

where, T is gas temperature and the subscript d represents dew point. In fact, even if no separation occurs, the partial pressure of water vapor and dew point at dry gas outlet will also decrease due to the gas expansion. Thus, the dew point depression ΔT_{d} at dry gas outlet should be divided into two parts, ΔT_{d1} due to expansion (without phase change) and ΔT_{d2} due to separation (with phase change), namely $\Delta T_{\text{d}} = \Delta T_{\text{d1}} + \Delta T_{\text{d2}}$. The effective dew point depression is ΔT_{d2} due to the condensation and separation.

The water removal rate η_{v} at dry gas outlet is calculated by

$$\eta_{\text{v}} = \frac{\chi_{\text{v}}^{\text{in}} - \chi_{\text{v}}^{\text{dry}}}{\chi_{\text{v}}^{\text{in}}} \times 100\% \tag{4}$$

where, χ is the mole fraction of water vapor and the subscript v represents the water vapor.

3. Mathematical model

3.1 Multi-fluid model for condensation-evaporation swirling flow

The multi-fluid model for condensation-evaporation swirling flow in supersonic separator was built according to the following assumptions: (i) The droplet is spherical; (ii) The released latent heat is completely absorbed by the gas phase due to the comparatively small heat capacity of droplet; (iii) both homogeneous and heterogenous condensations are considered; (iv) For the heterogenous condensation, the concentration $n_{\text{het}}^{\text{in}}$ and radius $r_{\text{het}}^{\text{in}}$ of the inlet foreign droplets (mainly contains water) are specified at the inlet; (v) The velocity slip between the gas and dispersed liquid phase is taken into account.

The mass conservation equation of the gas phase (humid gas) is expressed as

$$\frac{\partial \alpha_{\text{g}} \rho_{\text{g}}}{\partial t} + \frac{\partial}{\partial x_{\text{j}}}\left(\alpha_{\text{g}} \rho_{\text{g}} u_{\text{gj}}\right) = -\left(m_{\text{hom}} + m_{\text{het}}\right) \tag{5}$$

where the subscript g represent gas phase. α_{g}, ρ_{g} and u_{gj} are the volume fraction, density and mean velocity component of gas phase. $\alpha_{\text{g}} = 1 - \alpha_{\text{hom}} - \alpha_{\text{het}}$. The source items m_{hom} and m_{het} are liquid mass changing rates from homogenous and heterogenous condensations, respectively, kg m^{-3} s^{-1}. The momentum conservation equation of the gas phase is computed by

$$\frac{\partial \alpha_{\text{g}} \rho_{\text{g}} u_{\text{gi}}}{\partial t} + \frac{\partial}{\partial x_{\text{j}}}\left(\alpha_{\text{g}} \rho_{\text{g}} u_{\text{gi}} u_{\text{gj}}\right) = -\alpha_{\text{g}} \frac{\partial p}{\partial x_{\text{i}}} + \frac{\partial}{\partial x_{\text{j}}}\left[\alpha_{\text{g}} \mu_{\text{g}}\left(\frac{\partial u_{\text{gj}}}{\partial x_{\text{i}}} + \frac{\partial u_{\text{gi}}}{\partial x_{\text{j}}} - \frac{2}{3}\delta_{\text{ij}} \frac{\partial u_{\text{gk}}}{\partial x_{\text{k}}}\right)\right] + \frac{\partial}{\partial x_{\text{j}}}\left(-\alpha_{\text{g}} \rho_{\text{g}} \overline{u'_{\text{gi}} u'_{\text{gj}}}\right) - \left(m_{\text{hom}} + m_{\text{het}}\right) u_{\text{gi}} - F_{\text{Di}} \tag{6}$$

where μ_g is the dynamic viscosity of gas phase, i, j and k are tensor notations. u'_{gi} is the fluctuating component of the fluid velocity. F_{Di} is the component of drag force. δ_{ij} is the component of Kronecker delta. The energy conservation equation of the gas phase is described by

$$\frac{\partial \alpha_g \rho_g E}{\partial t} + \frac{\partial}{\partial x_j}\left[\alpha_g\left(\rho_g E + p\right)u_{gj}\right] = \frac{\partial}{\partial x_j}\left[\alpha_g\left(\lambda_{eff}\right)\frac{\partial T_g}{\partial x_j} + \alpha_g u_{gi}\left(\tau_{ij}\right)_{eff}\right] + \left(m_{hom} + m_{het}\right)h_{lg} \tag{7}$$

where the total energy is E and h_{lg} is the latent heat, J kg^{-1}. The effective turbulent thermal conductivity is $\lambda_{eff} = \lambda_g + \frac{c_{pg}\mu_{tu}}{\mathrm{Pr}_{tu}}$. The deviatoric stress tensor $\left(\tau_{ij}\right)_{eff}$ is defined by

$$\left(\tau_{ij}\right)_{eff} = \mu\left(\frac{\partial \bar{u}_{gj}}{\partial x_i} + \frac{\partial \bar{u}_{gi}}{\partial x_j}\right) - \frac{2}{3}\mu_{eff}\frac{\partial \bar{u}_{gk}}{\partial x_k}\delta_{ij} \tag{8}$$

where the effective turbulent viscosity is $\mu_{eff} = \mu + \mu_{tu}$ and the turbulent viscosity μ_{tu} is described by

$$\mu_{tu} = \frac{\rho_g k}{\omega}\frac{1}{\max\left[\frac{1}{a^*}, \frac{\Omega F_2}{a_1 \omega}\right]} \tag{9}$$

where k and ω are turbulence kinetic energy, J·kg^{-1} and specific dissipation rate, s^{-1}, respectively. The strain rate magnitude is $\Omega = \sqrt{2S_{i,j}S_{i,j}}$ and the component of mean strain rate $S_{i,j}$ is computed by $S_{i,j} = \frac{1}{2}\left(\frac{\partial \bar{u}_j}{\partial x_i} + \frac{\partial \bar{u}_i}{\partial x_j}\right)$. The coefficient a^* is a low-Reynolds number correction. a_1 is a constant 0.31. F_2 is the blending function.

The species transport equation for gas phase is expressed by

$$\frac{\partial}{\partial t}\left(\alpha_g \rho_g c_s\right) + \frac{\partial}{\partial x_j}\left(\alpha_g \rho_g u_j c_s\right) = \frac{\partial}{\partial x_j}\left(D_s \alpha_g \rho_g \frac{\partial c_s}{\partial x_j}\right) + S_{cs} \tag{10}$$

where c_s is the species mass fraction and D_s is mass diffusion coefficient. S_{cs} is source term in species transport equation. If the species is water vapor, S_{cs} = - (m_{hom} + m_{het}).

The turbulence kinetic energy and specific dissipation rate for gas phase are expressed as:

$$\begin{aligned}
&\frac{\partial}{\partial t}\left(\rho_g k\right) + \frac{\partial}{\partial x_j}\left(\rho_g k u_{gj}\right) = \frac{\partial}{\partial x_j}\left[\left(\mu + \frac{\mu_{tu}}{\sigma_k}\right)\frac{\partial k}{\partial x_j}\right] + G_k - Y_k \\
&\frac{\partial \rho_g \omega}{\partial t} + \frac{\partial}{\partial x_j}\left(\rho_g \omega u_{gj}\right) = \frac{\partial}{\partial x_j}\left[\left(\mu + \frac{\mu_{tu}}{\sigma_\omega}\right)\frac{\partial \omega}{\partial x_j}\right] + G_\omega - Y_\omega + D_\omega
\end{aligned} \tag{11}$$

where, G_k and G_ω are the generation of k and ω. Y_k and Y_ω are the dissipations of k and ω. D_ω is cross-diffusion term. σ_k and σ_ω are the turbulent Prandtl number.

The dispersed homogeneous and heterogeneous (foreign) droplet number concentrations n_{hom} and n_{het} (m^{-3}) are calculated by

$$\frac{\partial n_{hom}}{\partial t} + \frac{\partial}{\partial x_j}\left(n_{hom} u_{j,hom}\right) = J - n_{het} f \tag{12}$$

$$\frac{\partial n_{\mathrm{het}}}{\partial t}+\frac{\partial}{\partial x_{\mathrm{j}}}\left(n_{\mathrm{het}}u_{\mathrm{j,het}}\right)=0 \tag{13}$$

where, the subscripts hom and het represent homogenous and heterogenous. f is the mean collision frequency of one heterogenous droplet with others homogenous droplets. J is nucleation rate, $\mathrm{m^{-3}\ s^{-1}}$. The homogeneous and heterogeneous volume fraction α_{hom} and α_{het} are computed as follows,

$$\frac{\partial \alpha_{\mathrm{hom}}\rho_l}{\partial t}+\frac{\partial}{\partial x_{\mathrm{j}}}\left(\alpha_{\mathrm{hom}}\rho_l u_{\mathrm{j,hom}}\right)=m_{\mathrm{hom}}-n_{\mathrm{het}}f\rho_l\frac{4\pi r_{\mathrm{hom}}^3}{3} \tag{14}$$

$$\frac{\partial \alpha_{\mathrm{het}}\rho_l}{\partial t}+\frac{\partial}{\partial x_{\mathrm{j}}}\left(\alpha_{\mathrm{het}}\rho_l u_{\mathrm{j,het}}\right)=m_{\mathrm{het}}+n_{\mathrm{het}}f\rho_l\frac{4\pi r_{\mathrm{hom}}^3}{3} \tag{15}$$

where ρ_l is density of water droplet. Thus, the effective densities of homogenous and heterogenous droplet are

$$\rho_{\mathrm{hom}}=\alpha_{\mathrm{hom}}\rho_l,\qquad \rho_{\mathrm{het}}=\alpha_{\mathrm{het}}\rho_l \tag{16}$$

The velocity components $u_{\mathrm{j,hom}}$ and $u_{\mathrm{j,het}}$ for the homogenous and heterogenous droplets in liquid phases are calculated by

$$\frac{\partial \alpha_{\mathrm{hom}}\rho_l u_{\mathrm{i,hom}}}{\partial t}+\frac{\partial}{\partial x_{\mathrm{j}}}\left(\alpha_{\mathrm{hom}}\rho_l u_{\mathrm{i,hom}}u_{\mathrm{j,hom}}\right)=m_{\mathrm{hom}}u_{\mathrm{gi}}+F_{\mathrm{Di,hom}} \tag{17}$$

$$\frac{\partial \alpha_{\mathrm{het}}\rho_l u_{\mathrm{i,het}}}{\partial t}+\frac{\partial}{\partial x_{\mathrm{j}}}\left(\alpha_{\mathrm{het}}\rho_l u_{\mathrm{i,\ het}}u_{\mathrm{j,het}}\right)=m_{\mathrm{het}}u_{\mathrm{gi}}+F_{\mathrm{Di,het}} \tag{18}$$

where, $F_{\mathrm{Di,hom}}$ and $F_{\mathrm{Di,het}}$ are the components of drag force between the continuous and the dispersed phases.

3.2 Nucleation rate and droplet growth model

In this study, classical nucleation rate J ($\mathrm{m^{-3}\ s^{-1}}$) is calculated by [46]

$$J=\frac{\upsilon\rho_g^2}{S_{\mathrm{s}}}\sqrt{\frac{2\sigma}{\pi m_m^5}}\exp\left(-\frac{16\pi}{3}\frac{\upsilon^2\sigma^3}{\left(\mathrm{k_B}T_{\mathrm{g}}\right)^3\left(\ln S_{\mathrm{s}}\right)^2}\right) \tag{19}$$

where, υ, σ, m_{m} and $\mathrm{k_B}$ represent the volume of single water molecule ($\mathrm{m^3}$), liquid surface tension ($\mathrm{N\ m^{-1}}$), the mass of single water molecule (2.99×10^{-26} kg), and Boltzmann's constant (1.38×10^{-23} J $\mathrm{K^{-1}}$) respectively. The supersaturation of vapor is $S_{\mathrm{s}} = p_{\mathrm{v}} / p_{\mathrm{s}}(T_{\mathrm{g}})$, where $p_{\mathrm{s}}(T_{\mathrm{g}})$ is the water vapor saturation pressure at temperature T_{g}.

The critical nucleation radius r_{c} of the droplet is described by

$$r_{\mathrm{c}}=\frac{2\sigma}{\rho_l R_{\mathrm{v}}T_{\mathrm{v}}\ln\left(S_{\mathrm{s}}\right)} \tag{20}$$

where, R_{v} represent specific gas constant of water vapor. The mean radii r_{hom} and r_{het} are expressed as

$$r_{\mathrm{hom}}=\left(\frac{3\alpha_{\mathrm{hom}}}{4\pi n_{\mathrm{hom}}}\right)^{\frac{1}{3}},\qquad r_{\mathrm{het}}=\left(\frac{3\alpha_{\mathrm{het}}}{4\pi n_{\mathrm{het}}}\right)^{\frac{1}{3}} \tag{21}$$

Thus, the liquid mass changing rates m_{hom} and m_{het} are calculated by

$$m_{\mathrm{hom}}=J\rho_l\frac{4\pi r_c^3}{3}+n_{\mathrm{hom}}\rho_l 4\pi r_{\mathrm{hom}}^2\frac{dr_{\mathrm{hom}}}{dt},\quad m_{\mathrm{het}}=n_{\mathrm{het}}\rho_l 4\pi r_{\mathrm{het}}^2\frac{dr_{\mathrm{het}}}{dt} \tag{22}$$

The growth rate of droplet (both condensation and evaporation) is expressed as

$$\frac{dr}{dt}=\frac{\sum_{k=1}^{3}a_k}{\rho_l h_{lg}}\left(T_r-T_v\right) \tag{23}$$

where a_k is heat transfer coefficient. The subscript k represents different species in gas phase. The droplet surface temperature T_r is calculated by

$$T_r=T_d\left(p_v\right)-D_T\frac{r_c}{r} \tag{24}$$

where D_T is subcooling, = $T_d(p_v)$ - T_g. $T_d(p_v)$ is the dew point temperature at local water vapor pressure.

The flow inside the supersonic separator is strongly rotational and turbulent. The centrifugal acceleration can achieve 10^6 - 10^7 m s^{-2} [24]. The velocity slip between the gas and liquid phase has to be taken into account, for purpose of calculating the heat transfer coefficient accurately. The heat transfer coefficients a_k between the water droplet and each gas species are calculated by

$$a_k=\left(2+0.6\,\mathrm{Re}_p^{0.5}\,\mathrm{Pr}_g^{0.33}\right)\frac{\lambda_k}{2r}\frac{1}{1+\frac{2\sqrt{8\pi}}{1.5\,\mathrm{Pr}_k}\times\frac{\Gamma_k}{1+\Gamma_k}\mathrm{Kn}_k} \tag{25}$$

where Re_p, Γ, λ and Kn are Reynolds number, specific heat ratio, thermal conductivity and Knudsen number, respectively. For the water vapor, Kn is expressed as

$$\mathrm{Kn}_v=\frac{3\mu_v\sqrt{R_vT_g}}{4p_vr} \tag{26}$$

The relative Reynolds number $\mathrm{Re}_{p,\,het}$ is described as

$$\mathrm{Re}_{p,\,het}=2\rho_g r_{het}\left|\vec{u}_{het}-\vec{u}_g\right|\Big/\mu_g=2\rho_g r_{het}\left|Vs\right|\Big/\mu_g \tag{27}$$

where Vs is the slip velocity, = u_{het}-u_g. Besides, the liquid surface tension σ is calculated by [47]

$$\sigma=\left(85.27+75.612T_R-256.889T_R^2+95.928T_R^3\right)\times10^{-3} \tag{28}$$

where, T_R = T_g/T_c is the reduced temperature and T_c is critical temperature (647.3 K). The dew point temperature T_d is deduced by [48]

$$T_d=\begin{cases}2663.5\Big/\left(12.537-\lg p_v\right), & T_d\le 213.65\ \mathrm{K}\\ -60.45+7.0322\ln p_v+0.37\left(\ln p_v\right)^2+273.15, & 213.15\ \mathrm{K}\le T_d\le 273.15\ \mathrm{K}\\ -35.957-1.8726\ln p_v+1.1689\left(\ln p_v\right)^2+273.15, & T_d>273.15\ \mathrm{K}\end{cases} \tag{29}$$

The latent heat of vapor at the arbitrary temperature is computed by [49]

$$h_{lg}=h_{lg}^0\left(\frac{1-T_g/647.3}{1-0.5767}\right)^{0.38} \tag{30}$$

where the latent heat of water h_{lg} at the normal boiling point $h_{lg}{}^0$ is 2262.2 kJ·kg^{-1}.

3.3 Droplet coalescence and drag model

The mean collision frequency f of one heterogeneous foreign droplet (collector) with surrounding smaller homogeneous droplets is described by (O'Rourke [50])

$$f = n_{\text{hom}} \pi \left(r_{\text{het}} + r_{\text{hom}} \right)^2 u_{\text{rel}} \tag{31}$$

where $u_{\text{rel}} = |u_{\text{j,het}} - u_{\text{j,hom}}|$ is relative velocity between homogeneous and heterogeneous droplets. After the collisions, these smaller homogeneous droplets are collected by heterogeneous droplet, and the heterogeneous droplet radius increases up gradually. It is necessary to consider the effect of drag force in two-phase momentum equations for the swirling flow with strong centrifugal force. For smaller Reynolds numbers, the molecular viscous force dominates [51]. Thus, according to the Stokes' law, the drag force F_{D} is given by [52]

$$\vec{F}_{\text{D,hom}} = \frac{9\mu_{\text{g}}}{2r_{\text{hom}}^2 C_{\text{c}}} \alpha_{\text{hom}} \left(\vec{u}_{\text{g}} - \vec{u}_{\text{hom}} \right), \quad \vec{F}_{\text{D,het}} = \frac{9\mu_{\text{g}}}{2r_{\text{het}}^2 C_{\text{c}}} \alpha_{\text{het}} \left(\vec{u}_{\text{g}} - \vec{u}_{\text{het}} \right) \tag{32}$$

where, C_{c} is the empirical Cunningham slip correction factor which is calculated by

$$C_{\text{c}} = 1 + 2\text{Kn}_{\text{g}} \left(1.257 + 0.4 e^{-1.1/(2\text{Kn}_{\text{g}})} \right) \tag{33}$$

4. Experimental validation

4.1 Numerical implementation

All the cases were simulated by ANSYS FLUENT, while the governing equations and the source terms were performed with C code by the User-Defined-Scalar (UDS) and User-Defined-Function (UDF) interfaces. The density-based solver with implicit formulation and the Roe-FDS for flux type were utilized for calculating governing equations of multi-fluid flows including the gas and liquid phases. The second-order upwind scheme was employed for discretization. The gradients of flow variables for spatial discretization were calculated by the least squares cell based gradient evaluation. For turbulence model, the SST k-ω model was selected as the viscous model of gas phase. The structured quad-map meshes were utilized for better convergence. For inlet boundary conditions, the total temperature and pressure of fluid were given. The static pressure was set at the outlet. The concentration $n_{\text{het}}^{\text{in}}$ of inlet foreign droplet with a given radius $r_{\text{het}}^{\text{in}}$ were specified at the inlet. The constant-temperature condition which is equal to inlet gas temperature was enforced at walls. The solutions of density ρ_{g}, velocity u_{gj}, energy E, turbulence kinetic energy k, specific dissipation rate ω of the gas phase, the droplet concentration n_{hom} and n_{het}, the liquid phase effective density ρ_{hom} and ρ_{het}, the liquid velocity $u_{\text{j,hom}}$ and $u_{\text{j,het}}$ were converged to normalized residual mean square of 10^{-5}.

4.2 Experimental apparatus

This study mainly focuses on simulation analysis. The experiments are necessary to verify the accuracy of multi-fluid (slip) mathematical model. Thus, an experimental apparatus including a pure air generator, humidifier and acquisition controller [53] was built, as shown in Fig. 2. The pure air (dry gas) generator is composed of a compressor, a purifier, a gasholder, a self-operated pressure regulating valve and a motorized valve with feedback adjustment for controlling the pipeline pressure (0.1-0.6 bar, 0.2%) and flowrate (0.5-100 m^3/h, 0.5%). The gas temperature (30-50 ℃) is controlled by a tubular pipe heater with a silicon-controlled rectifier regulator. For controlling the relative humidity (0-100 %) of the moist

gas, the micron droplets are generated by a high-pressure micro-fog generator, and then evaporate within the evaporator to form the moist air at the upstream of the Laval nozzle and supersonic separator. A Vaisala HUMICAP humidity and temperature probe HMP110 is used to measure relative humidity and temperature. The light extinction method and image method are used to confirm that there is no any water droplet at the inlet. Then, the experimental data of 3D supersonic nozzle and supersonic separator can be used to validate the prediction accuracy of homogenous condensation in transonic flow and mass flow rate in swirling flow, respectively. For 3D supersonic nozzle, the time-averaged pressure signals along the axis of nozzle and the pressure fluctuation signals at a specific point near nozzle wall are measured by 12 pressure probes. For supersonic separator, its mass flow rate at different swirl strength are calibrated by a flow standard facility.

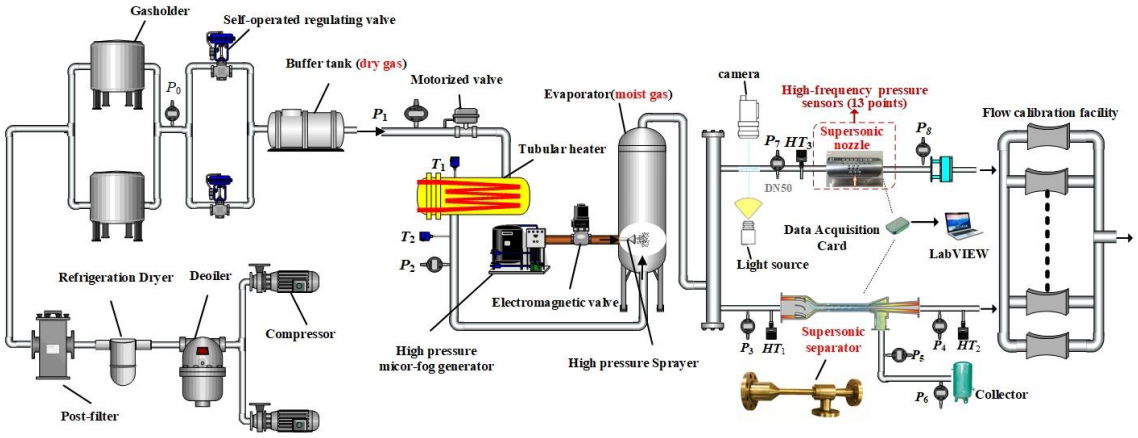

Fig. 2. The experimental apparatus for the nozzle and supersonic separator.

4.3 Model validation

Because the size of nozzle of supersonic separator is small and the swirling speed is fast, it is very difficult hard to measure condensation and swirling flow inside supersonic separator experimentally. Therefore, the validation of homogenous condensation and swirling flow are also performed by using supersonic nozzle and cyclone separator. Model validation can be divided into three steps. The first step is validation of homogenous condensation in a 2D nozzle and a 3D nozzle. The second step is validation of particle behavior in cyclone separator. The third step is validation of mass flow rate of gas through the supersonic separator. The experiments for model validation are shown in Table 1.

Table 1 The experiments for model validation.

Model validation	Device	Working fluid
Homogenous condensation in transonic flow	2D nozzle [54]	moist nitrogen
	3D nozzle	moist air
Particle behavior in swirling flow	Cyclone separator [55]	air
Mass flow rate in swirling flow	Supersonic separator	air

4.3.1 Condensation flow in Laval nozzle

The prediction accuracy of homogenous condensation process via the present CFD model was validated by some experiments in the Laval nozzle. The first validation was derived from Wyslouzil test [54] with a 2D nozzle where the working fluid is moist nitrogen. The length, inlet diameter and throat diameter of 2D nozzle are 133 mm, 40 mm and 12.7 mm with diffuser angle of 1.8° and the ratio of the outlet area to the throat area A^{out}/A^{nt} is 1.58. The inlet stagnation pressure p_*^{in} = 60.0 kPa and temperature T_*^{in} = 287 K with water vapor partial pressure p_v^{in} = 1.00, 0.50 and 0.26 kPa respectively.

A number of mesh tests were performed to guarantee a grid-independent solution. First, the effect of node numbers ($N_1 \times N_2$) was studied. The first procedure (N_1 fixed and N_2 varies) revealed that the mass flow rates with grid nodes 60 × 280, 60 × 300 and 60 × 320 are 1.781, 1.768 and 1.767 kg s^{-1} m^{-1} where the relative errors of two adjacent cases are -0.73% and -0.056%, and the mass-weighted average velocities at outlet are 465.379, 461.247 and 460.826 m/s where the relative errors of two adjacent cases are -0.98% and -0.091%, respectively. The second procedure (N_2 fixed and N_1 varies) revealed that the mass flow rates with grid nodes 50 × 300, 60 × 300 and 70 × 300 are 1.782, 1.768 and 1.765 kg s^{-1} m^{-1} where the relative errors are -0.79% and -0.17%, and the mass-weighted average velocities at outlet are 465.213, 461.247 and 460.740 m/s where the relative errors of two adjacent cases are -0.85% and -0.11%, respectively. Therefore, a grid size of 60×300 ensured a grid independent solution. The meshes near the throat and boundary layer were refined for better capturing the condensation and shock phenomena in the transonic flow, as show in Fig. 3 (a). It is observed that the numerical results of condensation-induced pressure jumps are in well agreement with the experimental data, as show in Fig. 3 (b). The present CFD model can predict 2D nonequilibrium condensation process in the transonic flow accurately.

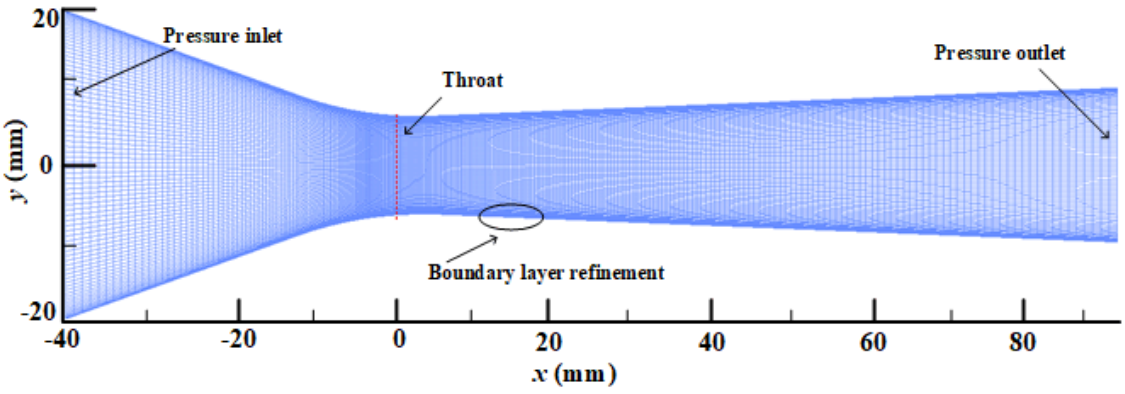

(a) The configuration and mesh of Laval nozzle

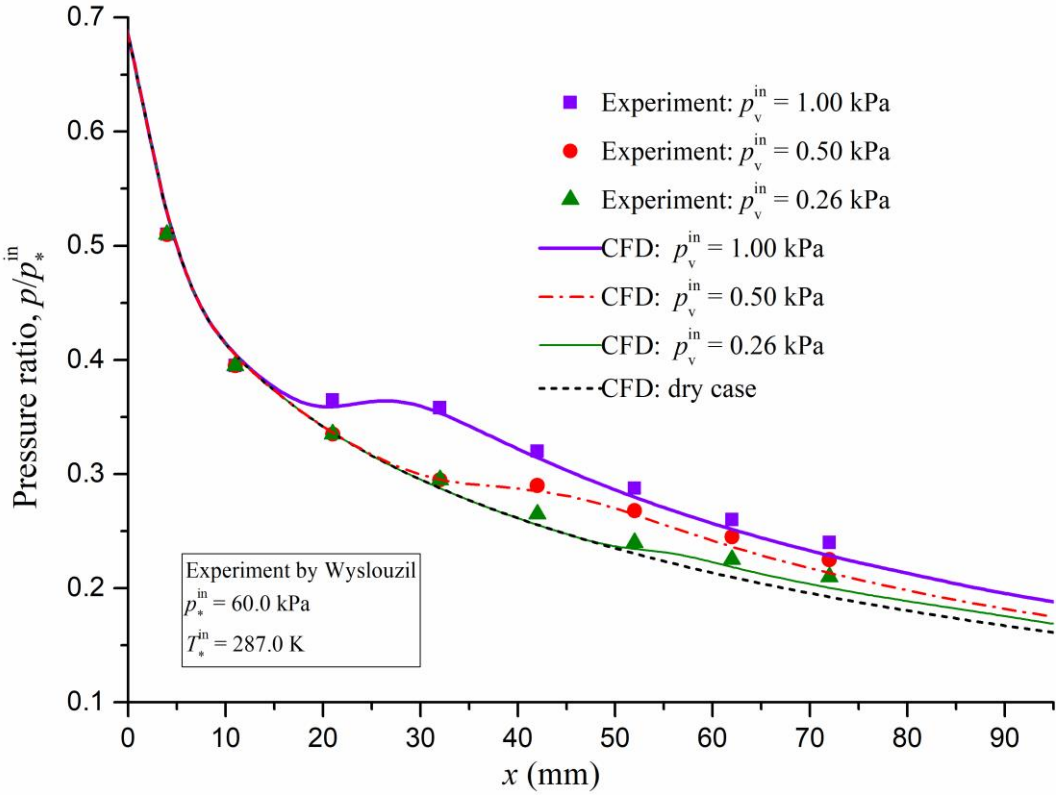

(b) The profiles of pressure ratio at the nozzle center downstream of nozzle throat

Fig. 3. Comparisons of CFD results with experimental data reported by Wyslouzil.

The second validation was performed in a 3D toroidal-throat supersonic nozzle with a throat diameter d of 10 mm and a curvature radius of 870 mm in our own experiment, as shown in Fig. 4. The grid of 3D nozzle is axisymmetric, thus, a series of grid independence analysis revealed that a grid size of 50×260 ensured a grid independent solution. The working fluid is moist air. In all cases, the inlet total pressure is 300 kPa and the static pressure at the outlet is 1 atm. The outlet static temperature is equal to the inlet value. The pressure profiles near the nozzle wall with different inlet relative humidity Φ^{in} and temperature T_*^{in} are shown in Fig. 5(a) and Fig. 5(b), respectively. It also indicates that CFD data are well consistent with experimental results. The pressure jump due to released latent heat inside the 3D supersonic nozzle was captured accurately.

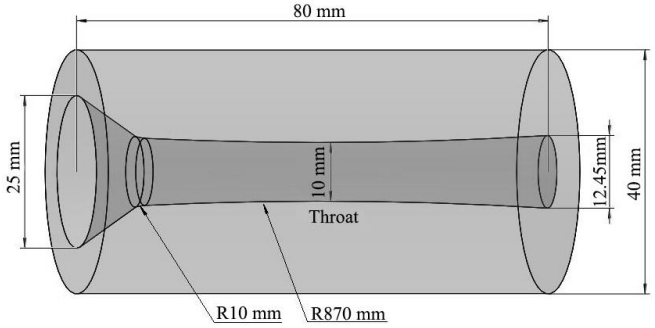

Fig. 4. The configuration of 3D toroidal-throat supersonic nozzle

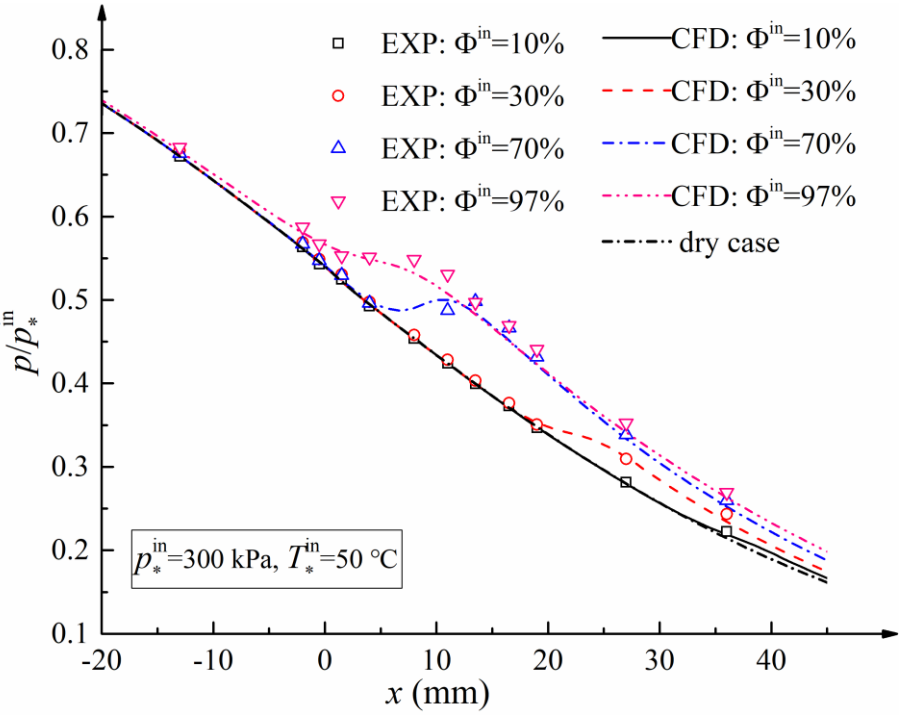

(a) Pressure profiles near the nozzle wall with different inlet relative humidity

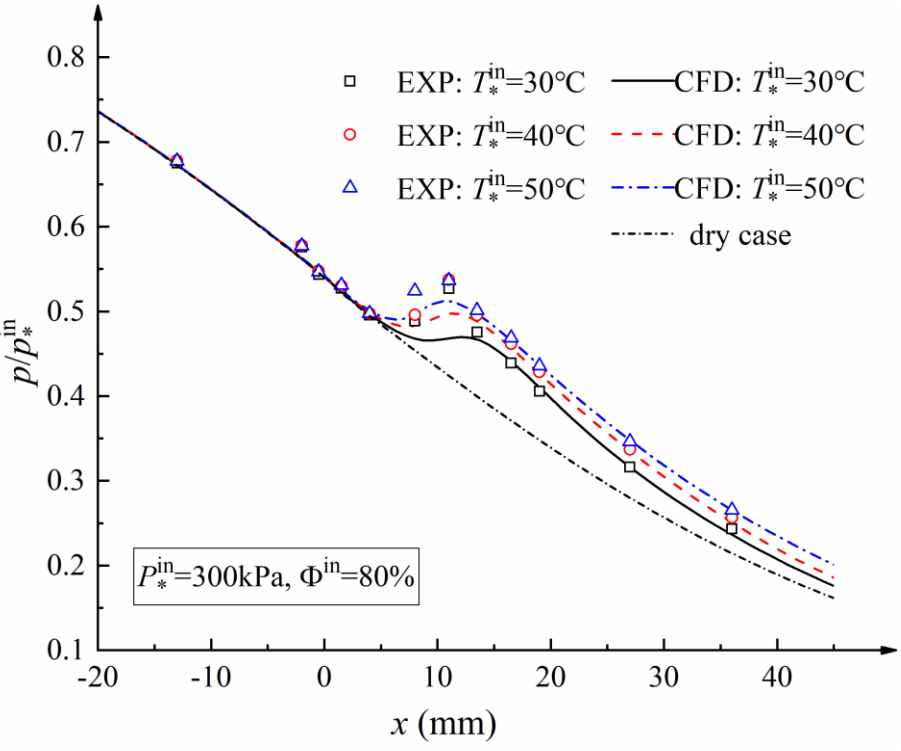

(b) Pressure profiles near the nozzle wall with different inlet temperature

Fig. 5. Comparisons of CFD results with our own experiments.

4.3.2 Particle behavior in the cyclone separators

To evaluate the simulation results of swirling flow by the present model, an experiment of a cyclone separator reported by Wang [55] was utilized. The configuration of the cyclone separator is shown in Fig. 6. A series of grid independence analysis revealed that the grid numbers of 53,468 ensured a grid independent solution. The working fluid is dry air where Φ_*^{in} = 0 %. The pressure at the top of vortex finder near the exit tube is 1 atm. The inlet velocity is 20 m s^{-1}. The solid particle material was a typical cement raw material with a concentration of 1%. The solid particle is equivalent to the inlet heterogeneous droplet of multi-fluid model without condensation. A comparison of the tangential velocity of gas flow field between the simulation and experiment is plotted in Fig. 7. A comparison of collection efficiency of particles between the simulation and experiment is plotted in Fig. 8. The simulation values agree well with the experimental data which indicates that the present model can predict behavior of particles in swirling flow very well.

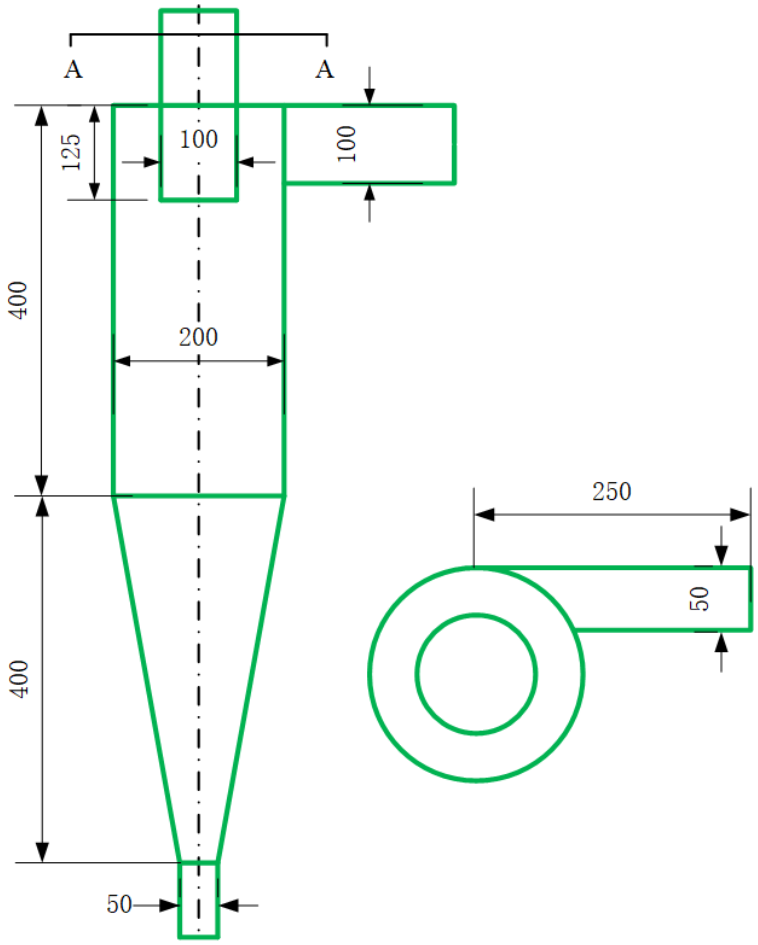

Fig. 6. Configuration of the cyclone separator (Unit: mm).

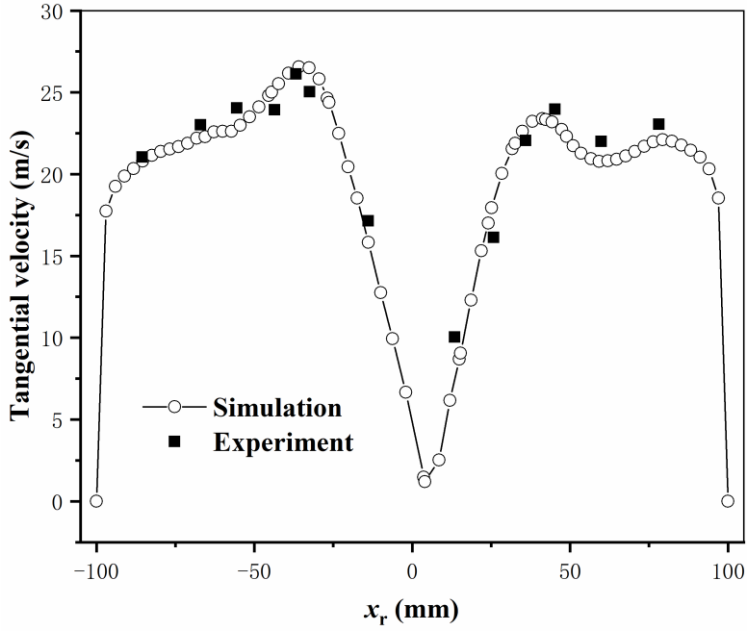

Fig. 7. Tangential velocity in a cyclone separator.

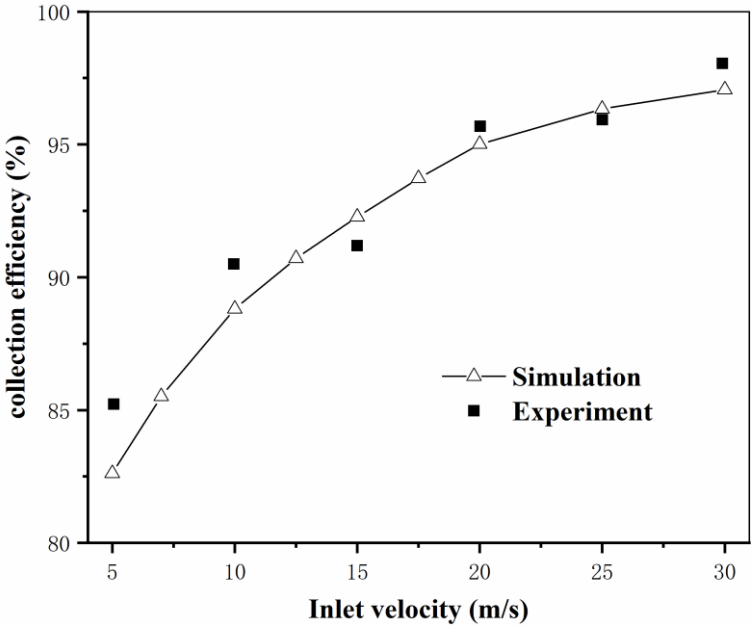

Fig. 8. Comparisons of collection efficiency between CFD results with experiment.

4.3.3 Mass flow rate in supersonic separator

The effects of swirl strength on the mass flow rate within a supersonic separator were also validated. The experimental data was derived from our experiment. The separator is 528 mm long, and has 70 mm/80 mm and 40 mm wall diameters at inlet and outlet. The diameters of the central body and the shell wall at the throat are 14 mm and 20 mm, respectively. The drainage gap size is about 2.0 mm. The only difference between supersonic separator A and B is the inlet diameter, separator A is 80 mm and separator

B is 70 mm.

The configuration and structured mesh of the supersonic separator A whose nominal swirl strength is 20% and the recovery of dry gas outlet is 0.72, are plotted in Fig. 9. A series of grid independence analysis revealed that the numbers of hexahedral meshes 576,300 ensured a grid independent solution. Besides, nominal swirl strength of supersonic separator B is 50%. The comparison of mass flow rates between simulation and experiment is shown in Fig. 10. The swirl strength S is defined as the ratio of the tangential velocity u_t to the axial velocity u_a (~ 318 m/s) at the throat. The dimensionless mass flow rate M is normalized by the mass flow rate with no swirling flow. It is found that the maximum error is about 2.7 % at the swirl strength of 93.4 %. It indicates that the proposed model predicts the strongly swirling supersonic flow accurately.

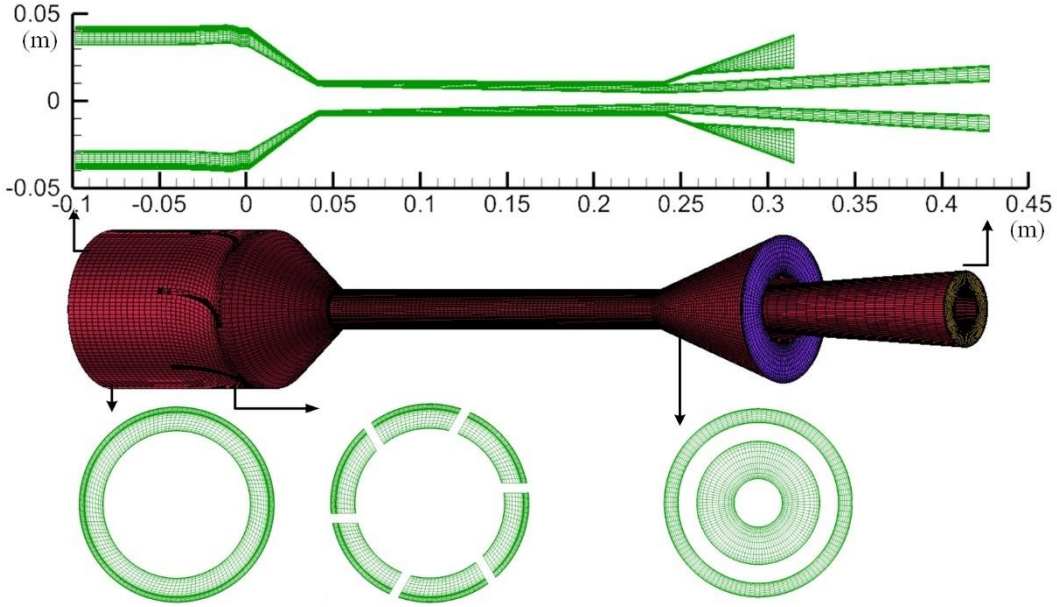

Fig. 9. The configuration and structured meshes of the supersonic separator A.

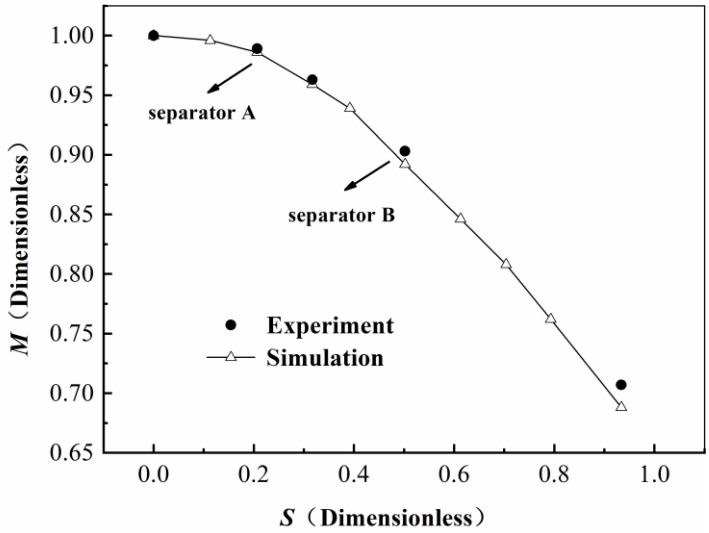

Fig. 10. The swirl strength effect on mass flow rate in the supersonic separator.

5. Results and discussion

Firstly, the detailed predictions for the gas and liquid (droplet) phases behaviors, especially for interphase velocity slip and liquid phase distribution are illustrated. Then, the results of dehydration performance (dew point depression ΔT_d and water removal rate η_v) of the supersonic separator at various conditions, i.e., total pressure, radius and concentration of inlet foreign droplet, and swirl strength were obtained.

5.1 Flow field, interphase slip and droplet behavior

Four cases were utilized to analyze the gas flow field, interphase slip and droplet behavior. The common conditions are T_*^{in} = 30 °C, Φ_*^{in} = 100% (p_v^{in} = 4246 Pa), p^{out} = 100 kPa, ρ_{het}^{in} = 0.01 kg m^{-3} (volume fraction $\alpha_{het}^{in} \approx 1\times10^{-5}$). The differences among these cases are as follows, Case 1-Case 3: p_*^{in} = 167, 200 and 250kPa (γ = 0.4 -0.6) with the same r_{het}^{in} = 1.0 μm and $n_{het}^{in} = 2.39\times10^{12}$ m^{-3}. Case 4: r_{het}^{in} = 0.4 μm with p_*^{in} = 250 kPa (γ = 0.6), and $n_{het}^{in} = 3.74\times10^{13}$ m^{-3}. If not specified, the supersonic separator A with nominal swirl strength S = 20% is assigned by default.

5.1.1 Shock wave and swirl strength

The sound speed in air-water two-phase mixture fluid can be calculated by (Wood' law [56])

$$c_{gl} = \sqrt{\frac{1}{\left(\alpha_g K_g^{-1} + \alpha_l K_l^{-1}\right)\left(\rho_g \alpha_g + \rho_l \alpha_l\right)}} \tag{34}$$

Where, α_g is volume fraction of gas, and α_l = 1-α_g is volume fraction of liquid, K is bulk elastic modulus. For liquid water, $K_l = 2.19\times10^4$ Pa. For ideal air gas, K_g = 1.4 p_g.

Another model proposed by Kieffer [57] is as follows

$$c_{gl} = \left(\beta\rho_{l,ref}\left(\frac{G_{g,ref}}{p}\right)^{1/\Gamma} + \exp\left(\frac{p_{ref}-p}{K_l}\right)\right)\left\{\left[(1+\beta)\rho_{l,ref}\right]^{1/2}\left[\frac{\beta\rho_{l,ref}G_{g,ref}^{1/\Gamma}}{\Gamma p^{(1+\Gamma)/\Gamma}} + \frac{1}{K_l}\exp\left(\frac{p_{ref}-p}{K_l}\right)\right]^{1/2}\right\}^{-1} \tag{35}$$

Where β is gas-liquid mass ratio. $G_{g,ref} = T_{ref} R_g/\rho_{ref}^{\Gamma-1}$. $\rho_{l,ref}$ and p_{ref} are chosen as 1000 kg/m^3 and 1 bar.

It is found that the results of Eq. (34) and Eq. (35) are almost same. However, it should be noticed that two-phase sound speed c_{gl} is sensitive to pressure. For case of p_*^{in} = 167 kPa, the minimum pressure inside supersonic separator is 56.098 kPa with T_g =290.67 K. if $\alpha_l = 6.5\times10^{-5}$, it shows c_g = 341.78 m s^{-1} and c_{gl} = 326.72 m s^{-1} where the error between them is 4.4 %. Thus, two-phase Mach number should be utilized to calculate Mach number, i.e. $Ma = u/c_{gl}$.

The Mach number contours for Case 1 and Case 3 inside the supersonic separator A are plotted in Fig. 11. It illustrates the complexity of shock wave, especially near the drainage channel. For Case 1 with smaller pressure loss (γ = 0.4) as shown in Fig. 11 (a), the maximum Mach number upstream of the shock is 1.239 at axial position x_a =91 mm, where the maximum subcooling D_T is 25.84 °C.

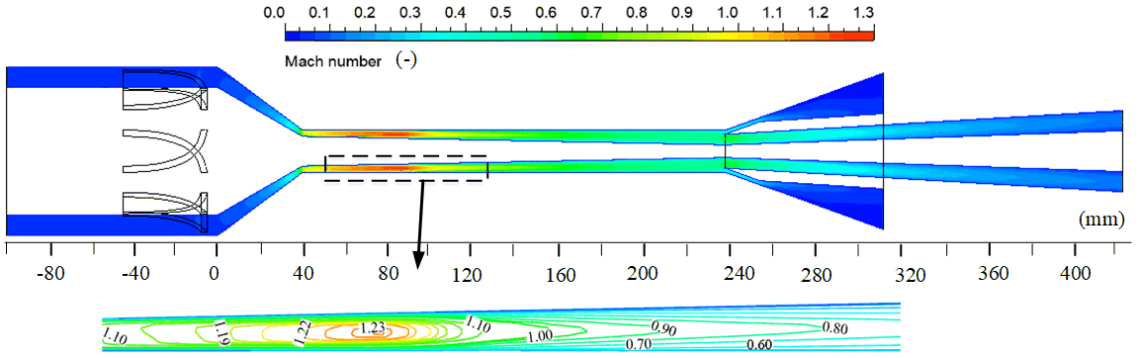

(a) Case 1: p_*^{in} = 167 kPa (γ = 0.4)

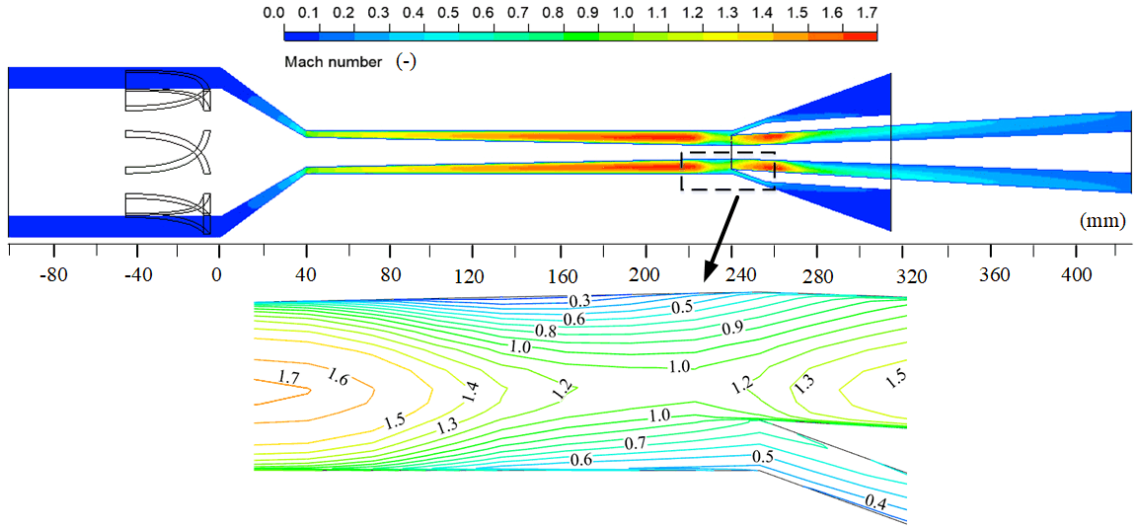

(b) Case 3: p_*^{in} = 250 kPa (γ = 0.6)

Fig. 11. The Mach number contours of the gas phase inside the supersonic separator.

On the other hand, when the inlet pressure increases up to 250 kPa, the shock wave will move downstream and reach the gas-liquid separation point with the maximum Mach number of 1.765 and subcooling D_T of 48.76 °C, as plotted in Fig. 11 (b). The fluid inside the drainage channel instantaneously reduces to subsonic speed, while the central fluid keeps supersonic and then a secondary shock occurs at the dry gas outlet channel. This complex shock is called lambda shock-system accompanying irreversible entropy production and loss of exergy [58].

The tangential velocity and swirl strength dominate the slip velocity and separation efficiency. However, the strong swirl strength decreases Mach number and increases the static temperature inside the Laval nozzle, damaging the expansion characteristics of the nozzle [24]. Fig. 12 (a) and (b) show the tangential velocities and streamlines of the gas phase for Case 3 in supersonic separators A and B. Fig. 12 (a) illustrates that the maximum tangential velocity in the separator A is u_t = 67.7 m s^{-1} and the maximum centrifugal acceleration is 8.70×10^5 m s^{-2} with swirl strength of 22%. In Fig. 12 (b), the maximum tangential velocity in the separator B reaches 136.1 m s^{-1} and the corresponding centrifugal acceleration is 3.5×10^6 m s^{-2} where the swirl strength achieves 45%. Then, the water vapor will be condensed and

separated from the non-condensable gas due to the low temperature and the strong centrifugal force.

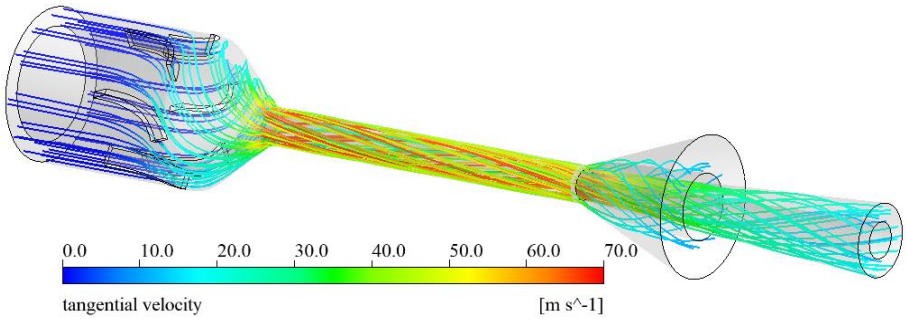

(a) Separator A: maximum tangential velocity is u_t = 67.7 m s^{-1}.

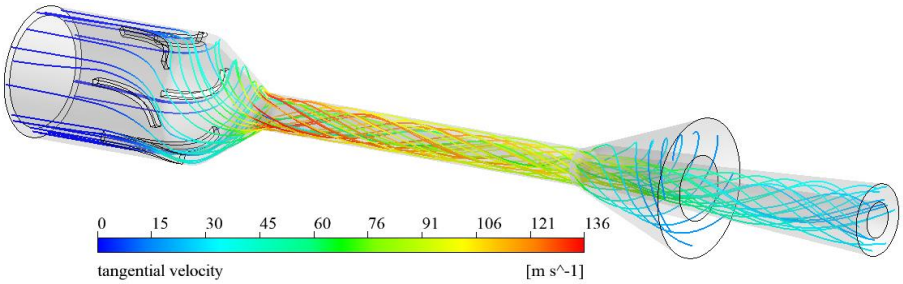

(b) Separator B: maximum tangential velocity is u_t =136.1 m s^{-1}.

Fig. 12. Tangential velocities and streamlines of the gas phase for Case 3 in separators A and B.

5.1.2 Condensation and evaporation zones

As we know, the water vapor will condense in the supersaturated region and the droplets will evaporate in the unsaturated region. As previously mentioned, both dry gas outlet and wet gas outlet are 100 kPa for Case 1 and Case 3. The heterogenous condensation is dominant and the homogenous condensation can be ignored in these two cases.

The contour of the liquid mass changing rate m_{het} for Case 1 when p_*^{in} = 167 kPa is plotted as Fig. 13 (a). It reveals that both condensation and evaporation processes occur inside the separator. The global range of the liquid mass changing rate m_{het} is from -402.3 to 712.1 kg m^{-3} s^{-1}. According to Fig. 11 (a), the shock occurs at axial position x_a = 91 mm which coincides with the evaporation onset. This is because the fluid velocity begins to slow down and the static temperature recovers to high value downstream of shock wave, and then droplets evaporate into the gas phase gradually.

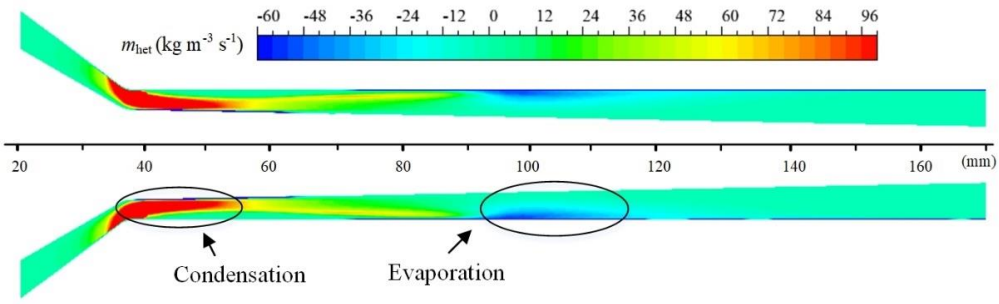

(a) at the core region for Case 1: p_*^{in} = 167 kPa (γ = 0.4)

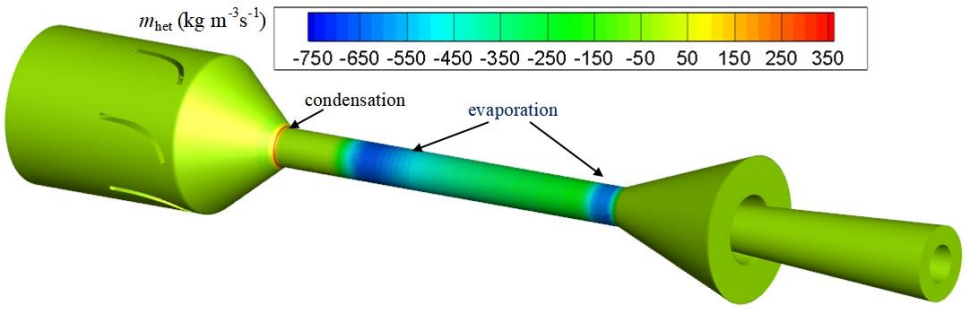

(b) at the near wall cells for Case 3: p_*^{in} = 250 kPa (γ = 0.6)

Fig. 13. The contours of the liquid mass changing rate m_{het} in the condensation and evaporation zones.

When the inlet pressure increases to 250 kPa, the rates of both condensation and evaporation are bigger. The global range of liquid mass changing rate m_{het} is from -936.7 to 958.3 kg m^{-3} s^{-1} (maximum latent heat release rate is 2.51×10^9 J m^{-3} s^{-1}). The liquid mass changing rate at the near wall cells are shown in Fig. 13 (b). It is found that the evaporation process occurs in two parts, the near-wall heating zone and pressure recovery zone.

For the purpose of demonstrating the condensation and evaporation processes, the distributions of the droplet radius and the vapor mass fraction along the axial direction are plotted in Fig. 14 and Fig. 15. The radial positions x_r of Line 1-Line 3 are 7 mm, 8 mm and 9 mm, respectively. Fig. 14 shows radius distributions of heterogenous droplet along Line 2 at different total pressures when inlet foreign droplets r_{het}^{in} = 1.0 μm, and ρ_{het}^{in} = 0.01 kg m^{-3}.

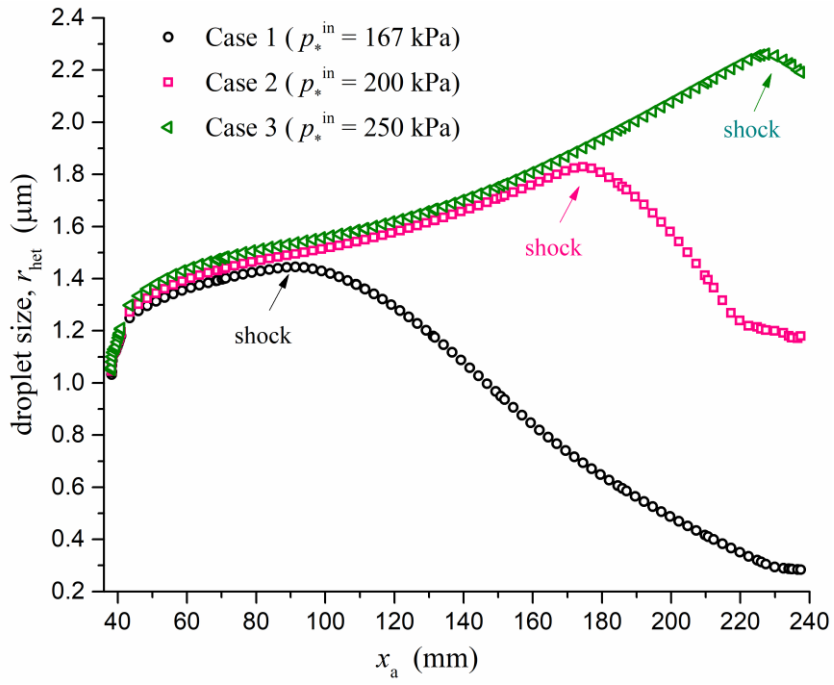

Fig. 14. The axial distributions of the droplet radius at Line 2 for Case 1, Case 2 and Case 3.

It indicates that the heterogenous droplet size starts growing rapidly at the throat. Along with the

increasing of heterogenous droplet size, its changing rate becomes smaller. The heterogenous droplet size will reach a maximum at the location of shock wave, and then begin to decrease due to the evaporation. The heterogenous droplet size grows to 1.44, 1.83 and 2.26 μm at x_a= 91.35, 174.50 and 227.40 mm for p_*^{in} = 167, 200 and 250 kPa.

The mass fraction of the water vapor in the gas phase also can reflect the changes of condensation and evaporation. Fig. 15 shows the results of mass fraction of water vapor for Case 3 with r_{het}^{in} = 1.0 μm and Case 4 with r_{het}^{in} = 0.4 μm. It is found that the mass fraction of water vapor at entrance of drainage will increase with the decrease of the inlet foreign droplet size, which means the smaller inlet foreign droplet radius r_{het}^{in} is, the worse dehydration performance is. The differences of performance are attributed to the interphase velocity slip and the uneven distribution of liquid phase.

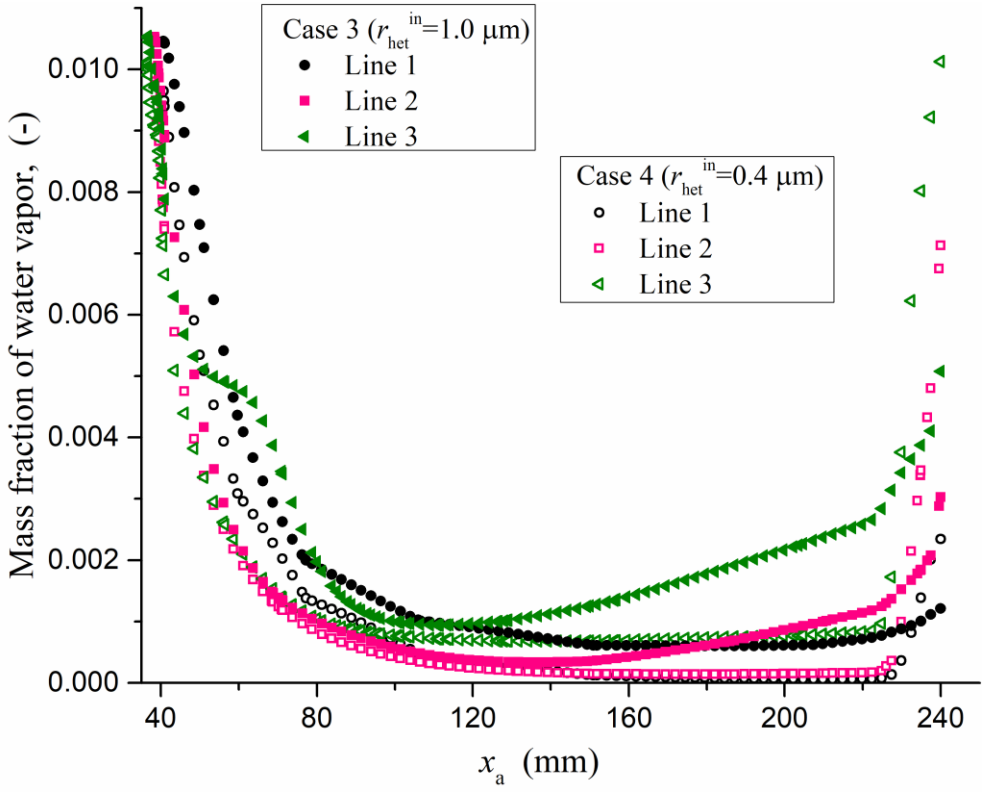

Fig. 15. The axial distributions of the mass fraction of water vapor for Case 3 and Case 4.

5.1.3 Slip velocity and Liquid phase distribution

The slip velocity and drag force play a critical role in controlling the trajectory of droplet which can determine the separation performance in the cyclone section. As the main factor, the effect of inlet foreign droplet radius on the slip velocity distribution is discussed firstly.

The axial and radial components of slip velocity at different locations of Case 3 and Case 4 are shown in Fig. 16. As shown in Fig. 16 (a), the magnitude of axial component of slip velocity decreases gradually along the flow direction where the maximum velocity lag of the droplet for x_a = 90, 140, and 190 mm is 48.2, 33.9 and 24.3 m s^{-1} as the result of the drag force. Besides, the axial slip velocity along

the radial direction is from zero (central inner body) to a negative minimum to zero again and then to positive maximum at the shell wall. Comparing Fig. 16 (a) and (c), it indicates that the bigger inlet droplet diameter is, the bigger droplet inertia is, and the larger slip speed will be. Fig. 16 (b) and (d) show the radial component of slip velocity at different locations. As we know, the radial slip speed causes the droplets to separate from primary gas fluid. It is obvious that the axial velocity of centrifugal droplet is larger than local velocity of gas phase. The maximum radial slip speed is 29.2 m s^{-1} for Case 3 and 8.26 m s^{-1} for Case 4.

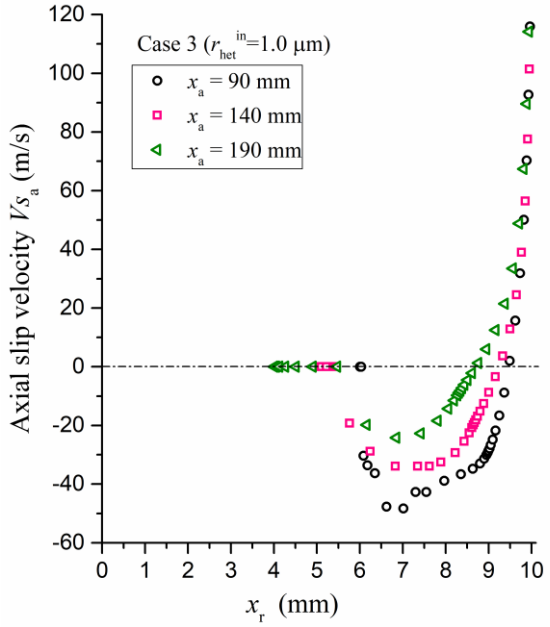

(a) Axial component of slip velocity for Case 3

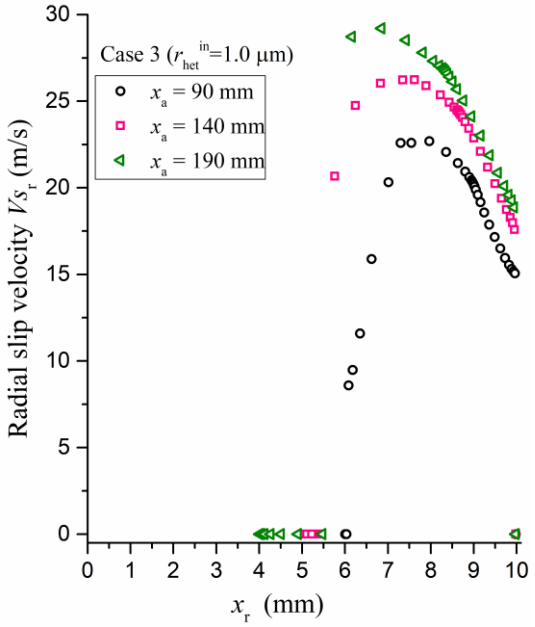

(b) Radial component of slip velocity for Case 3

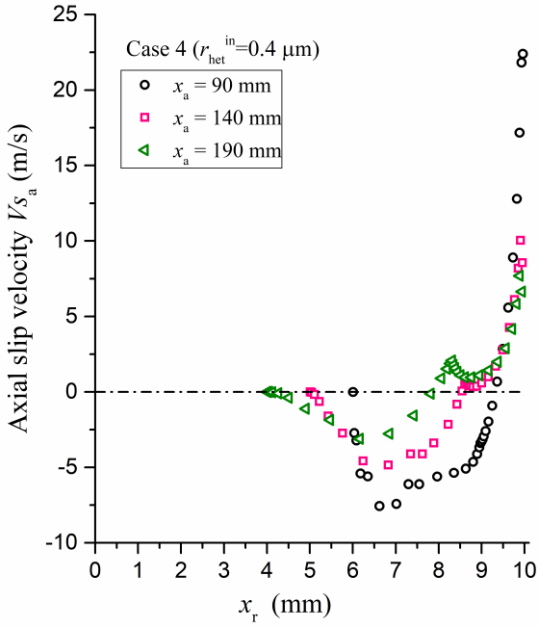

(c) Axial component of slip velocity for Case 4

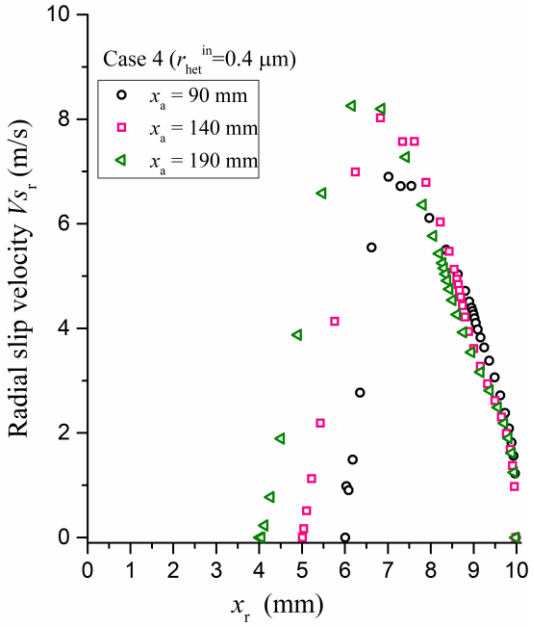

(d) Radial component of slip velocity for Case 4

Fig. 16. The axial and radial components of the slip velocity at different locations.

The distribution of liquid phase in the centrifugal field was analyzed. At first, the solution accuracy of the two-phase mass transfer was checked. Taking the results of Case 3 as example, the flow rate of inlet foreign droplets is Q_{het}^{in} = 2.75×10^{-4} kg s^{-1}. For the single-fluid model, inlet total mass flow rate of gas phase is Q_g^{in} = 7.83×10^{-2} kg s^{-1}, thus inlet mass flow rate of water vapor is Q_v^{in} = 8.32×10^{-4} kg s^{-1} because inlet mass fraction of water vapor is $c_{s,v}^{in}$ =1.063×10^{-2}. The outlet flow rate of water contains three parts, Q_{het}^{out} of heterogeneous droplets, Q_{hom}^{out} of homogeneous droplets and Q_v^{out} of vapor, where Q_{het}^{out} = 3.40 ×10^{-4} kg s^{-1}, Q_{hom}^{out} = 7.51 ×10^{-4} kg s^{-1} and Q_v^{out} = 2.4×10^{-5} kg s^{-1} at the gas-liquid separation section (x_a = 240 mm). The calculation error of total mass of water between the inlet and outlet is 0.72%. On the other hand, For the multi-fluid model, Q_g^{in} = 7.45×10^{-2} kg s^{-1} and Q_v^{in} = 7.92×10^{-4} kg s^{-1} at the inlet. The flow rates Q_{het}^{out} = 9.75 ×10^{-4} kg s^{-1}, Q_{hom}^{out} = 3.70×10^{-8} kg s^{-1} and Q_v^{out} = 1.01×10^{-4} kg s^{-1} at the outlet. The calculation error is 0.99 %. The results show a favorable prediction accuracy for two-phase mass transfer.

The streamline and effective density of heterogeneous droplets for Case 3 with r_{het}^{in} =1.0 μm by using both single-fluid and multi-fluid models are shown in Fig. 17. In single-fluid model, no-slip fluid velocity condition is assumed, thus the streamline of liquid phase goes around a circle at the cyclone as shown in Fig. 17 (a) and the effective density of heterogeneous droplet is almost uniform. Due to no slip in single-fluid model, the value of heat transfer coefficient of Eq. (25) is smaller than that of multi-fluid model. The droplet number of heterogenous droplet (n_{het}^{in} = 2.39×10^{12} m^{-3} in this case) is not usually enough to prevent the homogenous nucleation in single-fluid model. The percentages of heterogenous and homogenous condensations are 8% and 90%. When switching to the multi-fluid slip model, the streamline at the cyclone section is centrifugal motion as shown in Fig. 17 (b). The heat transfer coefficient around the heterogenous droplet sharply increases as a result of the interphase slip velocity. In this situation, the homogeneous condensation almost disappears. The effective density of heterogeneous droplet near the shell wall increase sharply due to the centrifugal force leading to the achievement of the separation performance.

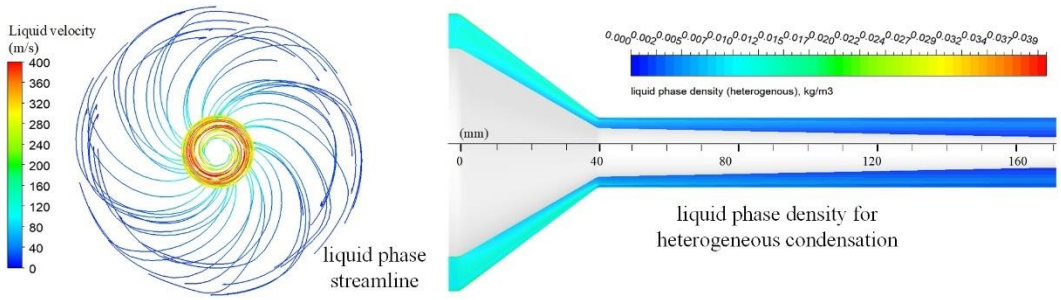

(a) Single-fluid (no-slip) model (8% heterogenous +90% homogeneous condensations at x_a = 240 mm)

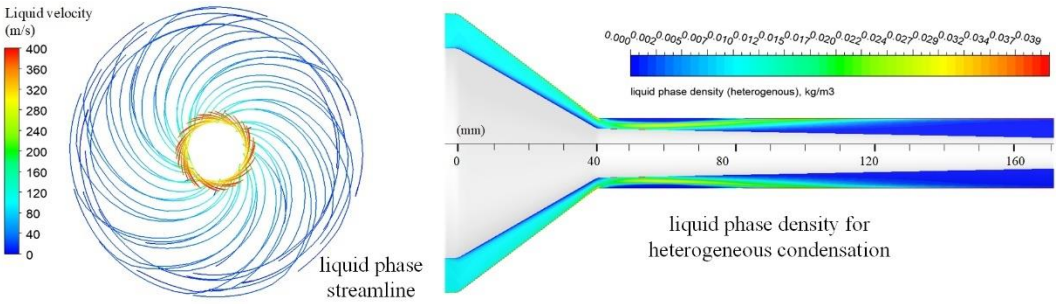

(b) Multi-fluid (slip) model (91% heterogenous + 0% homogeneous condensation at x_a = 240 mm)

Fig. 17. Comparisons of streamline and effective density of heterogeneous droplets between single-fluid model and multi-fluid model for Case 3.

Besides, the effective density contour of heterogeneous droplet for Case 4 with r_{het}^{in} = 0.4 μm by using multi-fluid model is plotted in Fig. 18. Compared with the contour of Case 3 with r_{het}^{in} = 1.0 μm in Fig. 17 (b), it reveals that the large droplet trajectory deflects faster than the small droplet as the result of the centrifugal force. However, if the droplet size is quite large, the residence time of heterogenous droplet in core flow will be too short which causes the insufficient heterogenous condensation and the failure of the separation. Thus, the inlet heterogenous droplet size should be moderate.

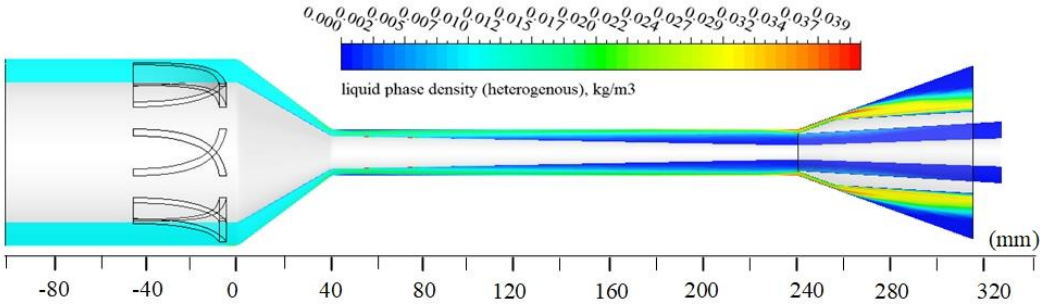

Fig. 18. Liquid phase effective density of heterogeneous condensation for Case 4.

5.2 Dehydration performance

The results of the dehydration performance of supersonic separator at different inlet conditions, when T_*^{in} = 30 °C, Φ_*^{in} = 100% (p_v^{in} = 4246 Pa) and p^{out} = 100 kPa, are shown in Table 2-Table 4. The variable p_v^{dry} is water vapor partial pressure at the dry gas outlet where the droplets evaporate again. T_d^{dry} and ΔT_d^{dry} represent the dew point and the dew point depression at the dry gas outlet.

Table 2 Dehydration performance of supersonic separator A with different r_{het}^{in} and ρ_{het}^{in} of inlet foreign droplets when p_*^{in} = 250 kPa (γ = 0.6).

r_{het}^{in} [μm]	ρ_{het}^{in} [kg m^{-3}]	n_{het}^{in} [m^{-3}]	p_v^{dry} [Pa]	T_d^{dry} [°C]	ΔT_d^{dry} [°C]	η_v
1.0	0.04	9.57×10^{12}	86.65	-21.71	51.71	94.90%
	0.02	4.78×10^{12}	130.62	-17.40	47.40	92.31%

	0.01	2.39×10^{12}	225.68	-11.48	41.48	86.71%
	0.005	1.20×10^{12}	348.99	-6.59	36.59	79.45%
	0.002	4.78×10^{11}	736.66	2.63	27.37	56.63%
	0.001	2.39×10^{11}	1197.13	9.49	20.51	29.53%
	0.0005	1.20×10^{11}	1532.67	13.19	16.81	9.77%
2.0	0.01	2.99×10^{11}	1319.60	10.93	19.07	22.32%
0.5		1.91×10^{13}	331.90	-7.16	37.16	80.46%
0.4		3.74×10^{13}	726.40	2.44	27.56	57.24%
0.3		8.86×10^{13}	1418.75	12.02	17.98	16.48%
0.25		1.53×10^{14}	1750.03	15.24	14.76	-3.02%
0.2		2.99×10^{14}	1999.98	17.34	12.66	-17.74%

Table 3 Dehydration performance of supersonic separator A with different r_{het}^{in} and ρ_{het}^{in} of inlet foreign droplets when p_*^{in} = 167 kPa (γ = 0.4).

r_{het}^{in} [μm]	ρ_{het}^{in} [kg m^{-3}]	n_{het}^{in} [m^{-3}]	p_v^{dry} [Pa]	T_d^{dry} [°C]	ΔT_d^{dry} [°C]	η_v [%]
1.0	0.04	9.57×10^{12}	2059.43	17.80	12.19	19.05%
	0.02	4.78×10^{12}	1571.55	13.58	16.42	38.20%
	0.01	2.39×10^{12}	1446.73	12.32	17.68	43.11%
	0.005	1.20×10^{12}	1483.44	12.69	17.31	41.66%
	0.002	4.78×10^{11}	1694.78	14.74	15.26	33.35%
	0.001	2.39×10^{11}	2113.84	18.22	11.78	16.87%
	0.0005	1.20×10^{11}	2387.42	20.19	9.80	6.13%
2.0	0.01	2.99×10^{11}	2027.67	17.56	12.44	20.26%
1.5		7.09×10^{11}	1539.66	13.26	16.74	39.45%
0.75		5.67×10^{12}	1831.56	15.95	14.05	27.97%
0.5		1.91×10^{13}	2241.32	19.17	10.83	11.86%
0.3		8.86×10^{13}	2984.91	23.89	6.10	-17.43%
0.2		2.99×10^{14}	3368.58	25.95	4.05	-32.47%

Fig. 19 shows the curves of the dew point depression ΔT_d^{dry} versus inlet foreign droplet size r_{het}^{in} when p_*^{in} = 167 and 250 kPa, where ΔT_{d1}^{dry} due to expansion at dry gas outlet are 8.77 and 15.22 °C, respectively. It is observed that there is an optimal radius of inlet foreign droplets to maximize the dehumidification and efficiency of the device. For p_*^{in} = 250 kPa, the maximum of ΔT_d^{dry} is 42.41°C (η_v = 87.82%) at the optimal radius r_{het}^{in} of 0.85 micron, while for p_*^{in} = 167 kPa, the maximum of ΔT_d^{dry} is 17.52°C (η_v = 42.50%) at the optimal radius r_{het}^{in} of 1.25 micron. The residence time of droplet is the main factor leading to above result which was explained clearly in Fig. 17 (b) and Fig. 18.

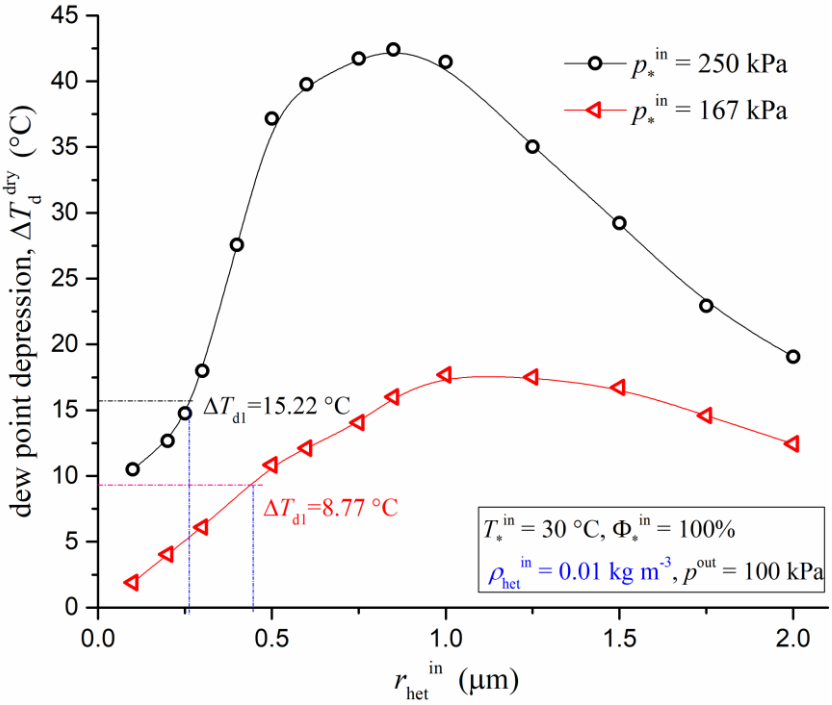

Fig. 19. The dew point depression ΔT_d versus inlet foreign droplet size r_{het}^{in} when p_*^{in} = 167 and 250 kPa.

In addition, as shown in Table 2-Table 3 and Fig. 19, when the inlet foreign droplet size is less than a critical size, the dew point depression ΔT_d^{dry} will be smaller than ΔT_{d1}^{dry} where the water removal rate η_v is negative, the separator would be ineffective. The critical sizes of r_{het}^{in} are 0.26 micron and 0.45 micron for p_*^{in} = 250 and 167 kPa, respectively. When the inlet foreign droplet size continues to decrease, it will begin to evaporate into the gas phase instead of condensing, thus the water vapor partial pressure at the dry gas outlet increases and the removal rate η_v is negative, resulting in the failure of separation.

The values of dew point depression ΔT_d^{dry} at different inlet effective densities ρ_{het}^{in} are shown in Fig. 20. It is found that the curve is monotonically increasing with the ρ_{het}^{in} for p_*^{in} = 250 kPa, where the shock wave is near the entrance of drainage as shown in Fig. 11 (b) and the evaporation is weak. On the other hand, the curve has a maximum ΔT_d^{dry} at the optimal effective density of 0.008 kg m^{-3} for p_*^{in} = 167 kPa. In this situation, the evaporation zone is quite long at the downstream of the shock shown in Fig. 11 (a) and Fig. 13 (a). Although the water vapor is condensed completely at the condensation zone, it re-evaporates again after the shock. When ρ_{het}^{in} is larger than the optimal value, the amount of condensation remains the same but the evaporation increases gradually with the increase of ρ_{het}^{in}, resulting in the reduction of the dehydration performance.

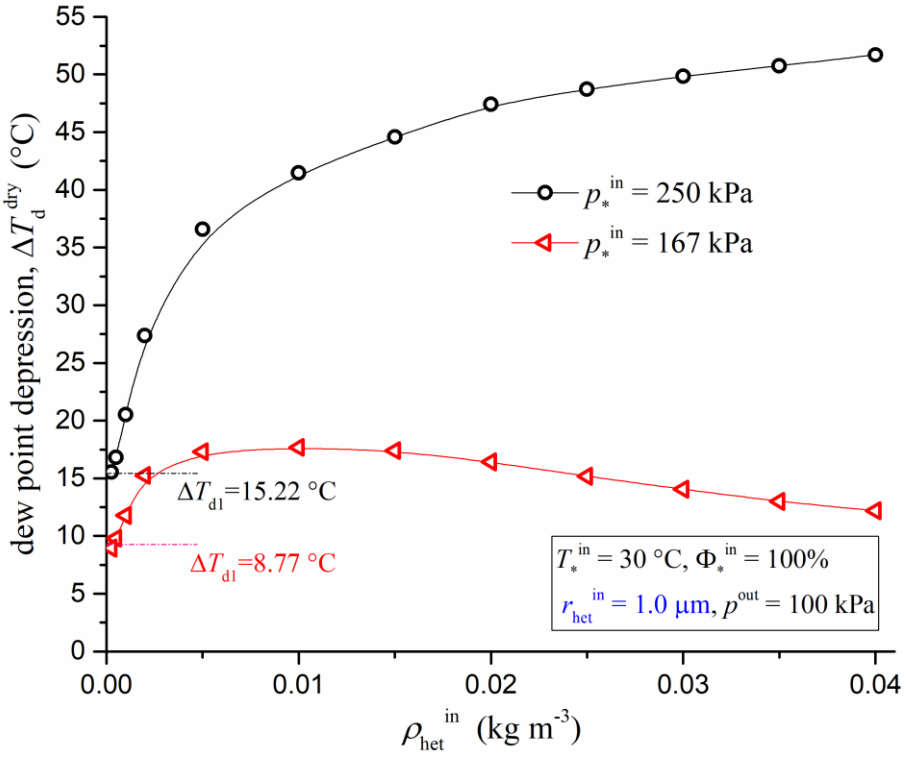

Fig. 20. The dew point depression ΔT_d versus effective density ρ_{het}^{in} of inlet foreign droplets when p_*^{in} = 167 and 250 kPa.

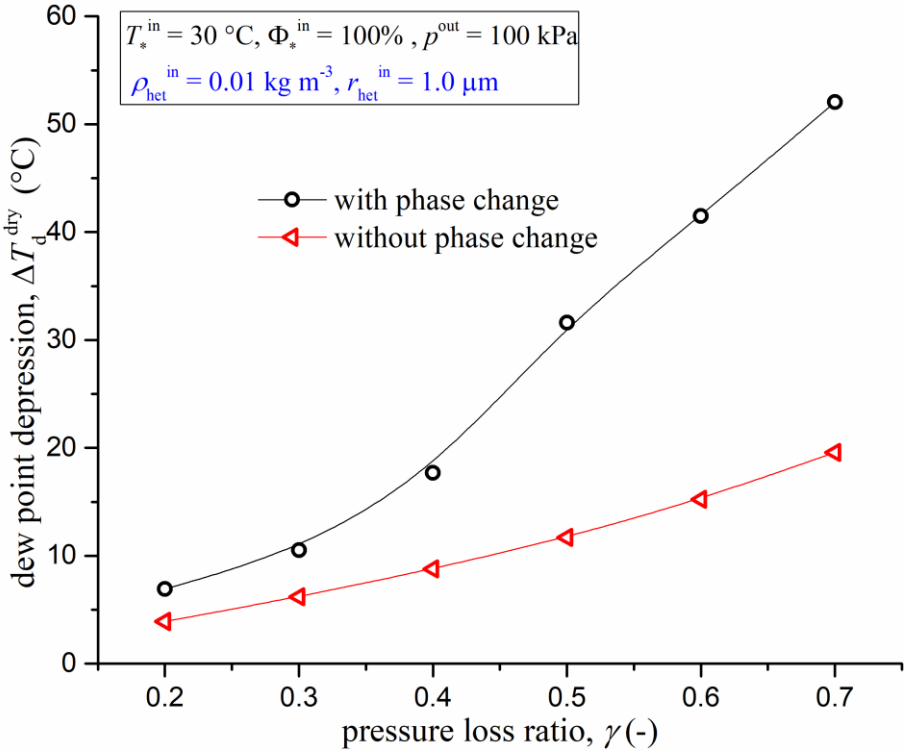

Fig. 21. The dew point depression ΔT_d versus the pressure loss ratio γ when inlet heterogenous conditions are ρ_{het}^{in} = 0.01 kg m^{-3} and r_{het}^{in} = 1.0 μm.

Fig. 19 and Fig. 20 also illustrate the supersonic separator will provide better dehydration performance if the pressure loss ratio increases. The dew point depression ΔT_d versus the pressure loss ratio γ is plotted in Fig. 21. The original data of Fig. 21 is also listed in Table 4. It reveals that the dew point depression ΔT_d^{dry} increases from 6.91 °C (η_v = 16.23%) to 52.04 °C (η_v = 93.42%) when the pressure loss ratio increases up to 0.7. The larger the pressure loss ratio inputs, the higher the separation efficiency will be. However, high pressure loss ratio means high energy consumption.

Table 4 Dehydration performance of supersonic separator A with different pressure loss ratio γ when r_{het}^{in} = 1.0 μm and ρ_{het}^{in} = 0.01 kg m^{-3} (n_{het}^{in} = 2.39×10^{12} m^{-3}).

γ [-]	p_*^{in} [kPa]	p_v^{dry} [Pa]	T_d^{dry} [°C]	ΔT_d^{dry} [°C]	ΔT_{d1}^{dry} [°C]	η_v [%]
0.7	333	83.85	-22.04	52.04	19.58	93.42%
0.6	250	225.64	-11.48	41.48	15.22	86.71%
0.5	200	538.01	-1.60	31.60	11.70	74.66%
0.4	167	1449.39	12.32	17.68	8.77	43.11%
0.3	133	2285.62	19.48	10.52	6.19	23.10%
0.2	125	2845.51	23.09	6.91	3.91	16.23%

Besides, the effect of swirl strength on the separation efficiency was also investigated. The dehydration performance of supersonic separator B with 45% swirl strength is shown in Table 5. The optimal size of inlet foreign droplets for heterogenous condensation is 0.28 micron. Compared with the results of separator A with 22% swirl strength in Table 2, it is found that the optimal radius of inlet foreign droplets will be smaller when the separator has a stronger swirl strength. These results are helpful for designing the separator structure and optimizing the separation performance.

Table 5 Dehydration performance of supersonic separator B with different r_{het}^{in} of inlet foreign droplets when ρ_{het}^{in} =0.01 kg m^{-3} and p_*^{in} = 250 kPa (γ = 0.6).

r_{het}^{in} [μm]	n_{het}^{in} [m^{-3}]	p_v^{dry} [Pa]	T_d^{dry} [°C]	ΔT_d^{dry} [°C]	η_v
1.0	2.39×10^{12}	1619.10	14.03	15.97	4.68%
0.75	5.67×10^{12}	1075.83	7.93	22.07	36.67%
0.5	1.91×10^{13}	542.49	-1.57	31.57	68.06%
0.4	3.74×10^{13}	275.71	-9.25	39.25	83.77%
0.3	8.86×10^{13}	103.48	-19.86	49.86	93.91%
0.25	1.53×10^{14}	116.45	-18.65	48.65	93.14%
0.2	2.99×10^{14}	370.46	-5.91	35.91	78.19%
0.15	7.01×10^{14}	1045.34	7.52	22.48	38.46%
0.1	2.39E×10^{15}	1685.87	14.66	15.34	0.75%

6. Conclusion

A novel multi-fluid model with the droplet coalescence and the interphase force for the homogenous/heterogenous condensation and evaporation processes in supersonic separator was built to

evaluate the dehydration performance. The flow field, slip velocity profile, droplet trajectory and liquid phase distribution with different pressure loss ratios, the radii and concentrations of inlet foreign droplets were analyzed. The dehydration performances were also investigated further. The conclusions are as follows:

(1) The complex lambda shock-system with maximum Mach number of 1.765 and subcooling of 48.76 °C was observed in the cyclone section, where the maximum tangential velocity was 136.1 m s^{-1} and the corresponding centrifugal acceleration was 3.5×10^6 m s^{-2}.

(2) The condensation begins to occur at the throat, while the evaporation appears at the near-wall heating and pressure recovery zones. The liquid mass changing rate m_{het} ranges from -936.7 to 958.3 kg m^{-3} s^{-1} with latent heat release rate of 2.51×10^9 J m^{-3} s^{-1}. When r_{het}^{in} = 1.0 μm, and ρ_{het}^{in} = 0.01 kg m^{-3}, the heterogenous droplet size grows to 1.44, 1.83 and 2.26 micron for p_*^{in} = 167, 200 and 250 kPa.

(3) The magnitude of axial component of slip velocity decreases gradually along the flow direction where maximum velocity lag of the droplet is 48.2 m s^{-1} for r_{het}^{in} = 1.0 μm. The maximum values of radial slip velocity are 29.2 m s^{-1} for r_{het}^{in} = 1.0 μm and 8.26 m s^{-1} for r_{het}^{in} = 0.4 μm, respectively. It is indicated that the larger foreign droplet will grow faster due to the enhanced heat transfer coefficient.

(4) However, large droplet will deflect faster resulting in a shorter residence time and failure of separation. Thus, the inlet foreign droplet radius should be moderate for the best performance.

(5) There is an optimal size of inlet foreign droplet to maximize dehumidification and efficiency. When p_*^{in} = 250 kPa and ρ_{het}^{in} = 0.01 kg m^{-3}, the optimal radii of inlet foreign droplet are 0.85 and 0.28 micron in two different separators, in which the maximum dew point depression ΔT_d^{dry} is 42.41 °C and water removal rate η_v is 87.82% in separator A while maximum ΔT_d^{dry} = 48.65 °C and η_v = 93.91% are valid for separator B.

This study provides an insight into dehydration performance of the supersonic separator considering the condensation, evaporation and interphase force. For future work, it is important to optimize the structure of supersonic separator by using present model and investigate experimentally the water separation efficiency of supersonic separator via heterogeneous condensation.

Conflict of interest

The authors declared that there is no conflict of interest.

Acknowledgement

This research is supported by National Natural Science Foundation of China under Grant 51876143, 61873184, and 61627803, European Union's Horizon 2020 research and innovation programme under the Marie Sklodowska-Curie grant agreement No 792876.

References

[1]. Khan MI, Shahrestani M, Hayat T, Shakoor A, Vahdati M. Life cycle (well-to-wheel) energy and

environmental assessment of natural gas as transportation fuel in Pakistan. Appl Energy 2019;242:1738-52.

[2]. Interlenghi SF, Raquel de Pádua FS, de Medeiros JL, Araújo OQF. Low-emission offshore Gas-To-Wire from natural gas with carbon dioxide: Supersonic separator conditioning and post-combustion decarbonation. Energ Convers Manage 2019;195:1334-49.

[3]. Liu, X, Liu Z. Investigation of the energy separation effect and flow mechanism inside a vortex tube. Appl Therm Eng 2014;67:494-506.

[4]. Wen C, Karvounis N, Walther JH, Yan Y, Feng Y, Yang Y. An efficient approach to separate CO2 using supersonic flows for carbon capture and storage. Appl energy 2019;238:311-9.

[5]. Machado PB, Monteiro JGM, de Medeiros JL, Epsom HD, Araujo OQF. Supersonic separation in onshore natural gas dew point plant. J Nat Gas Sci Eng 2012;6:43-9.

[6]. Li S, Deng S, Zhao L, Zhao R, Lin M, Du Y, Lian Y. Mathematical modeling and numerical investigation of carbon capture by adsorption: Literature review and case study. Appl Energy 2018;221:437-49.

[7]. Yang Y, Walther JH, Yan Y, Wen C. CFD modeling of condensation process of water vapor in supersonic flows. Appl Therm Eng 2017;115:1357–62.

[8]. Eriqitai, Han J, Duan R, Wu M, 2014. Performance of dual-throat supersonic separation device with porous wall structure. Chin J Chem Eng 2014;22(4):370-82.

[9]. Haghighi M, Hawboldt KA, Abdi MA. Supersonic gas separators: Review of latest developments. J Nat Gas Sci Eng 2015;27:109-21.

[10]. Cao X, Bian J. Supersonic separation technology for natural gas processing: A review. Chem Eng Process 2019;136:138-51.

[11]. Teixeira AM, Arinelli LO, de Medeiros JL, Araújo OQF, Economic leverage affords post-combustion capture of 43% of carbon emissions: Supersonic separators for methanol hydrate inhibitor recovery from raw natural gas and CO2 drying. J Env Manag 2019;236:534-550.

[12]. Karimi A, Abdi MA. Selective dehydration of high-pressure natural gas using supersonic nozzles. Chem Eng Process 2009;48:560-8.

[13]. Wen C, Cao X, Yang Y, Li W. An unconventional supersonic liquefied technology for natural gas. Energy Educ Sci Technol Part A Energy Sci Res 2012;30: 651-660.

[14]. Hammer M, Wahl PE, Anantharaman R, Berstad D, Lervåg KY, CO2 capture from off-shore gas turbines using supersonic gas separation. Energy Procedia 2014;63:243-252.

[15]. Niknam PH, Mortaheb HR, Mokhtarani B. Optimization of dehydration process to improve stability and efficiency of supersonic separation. J Natural Gas Sci Eng 2017;43:90-95.

[16]. Niknam PH, Mortaheb HR, Mokhtarani B. Effects of fluid type and pressure order on performance of convergent-divergent nozzles: An efficiency model for supersonic separation. Asia-Pacific J Chem Eng 2018;13(2):1932-2135.

[17]. Arinelli LO, Trotta TAF, Teixeira AM, de Medeiros JL, Araújo OQF. Offshore processing of CO2 rich natural gas with supersonic separator versus conventional routes. J Natural Gas Sci Eng 2017;46:199-221.

[18]. Bian J, Cao X, Yang W, Edem MA, Yin P, Jiang W. Supersonic liquefaction properties of natural gas in the Laval nozzle. Energy, 2018;159:706-715.
[19]. an N, Jamil H, Shirazian S. Process simulation and evaluation of ethane Rezakazemi M, Rahmanirecovery process using Aspen-HYSYS, Chem Eng Trans 2018;70:961-966.
[20]. Brigagão GV, Arinelli LO, de Medeiros JL, Araújo OQF. A new concept of air pre-purification unit for cryogenic separation: low-pressure supersonic separator coupled to finishing adsorption. Sep Purif Technol 2019;215:173-189.
[21]. de Medeiros JL, Arinelli LO, Araújo OQF. Speed of sound of multiphase and multi-reactive equilibrium streams: A numerical approach for natural gas applications. J. Nat. Gas. Sci. Eng. 2017;46:222-41.
[22]. de Medeiros JL, Arinelli LO, Teixeira AM, Araújo OQF. Offshore processing of CO2-rich natural gas with supersonic separator: multiphase sound speed, CO2 freeze-out and HYSYS implementation. Springer Int. Publishing, 2019.
[23]. Malyshkina M. The procedure for investigation of the efficiency of purification of natural gases in a supersonic separator. High Temp 2010;48:244-50.
[24]. Wen C, Cao X, Yang Y, Zhang J. Swirling effects on the performance of supersonic separators for natural gas separation. Chem Eng Technol 2011;34(9):1575-80.
[25]. Wen C, Cao X, Yang Y, Feng Y. Prediction of mass flow rate in supersonic natural gas processing. Oil Gas Sci Technol 2015;70:1101-9.
[26]. WangY, Hu D. Experimental and numerical investigation on the blade angle of axial-flow swirling generator and drainage structure for supersonic separators with diversion cone. Chem Eng Res Des 2018;133:155-167.
[27]. Liu X, Liu Z. Numerical investigation and improvement strategy of flow characteristics inside supersonic separator. Sep Sci Technol. 2018: 53(6):940-52.
[28]. Alnoush W, Castier M. Shortcut modeling of natural gas supersonic separation. J Nat Gas Sci Eng 2019;65:284-300.
[29]. Wen C, Cao X, Yang Y, Zhang J. Evaluation of natural gas dehydration in supersonic swirling separators applying the discrete particle method. Adv Powder Technol 2012;23:228-33.
[30]. Yang Y, Wen C. CFD modeling of particle behavior in supersonic flows with strong swirls for gas separation. Sep Purif Technol 2017;174:22-8.
[31]. Liu X, Liu Z, Li Y. Investigation on separation efficiency in supersonic separator with gas-droplet flow based on DPM approach. Sep Sci Technol 2014;49:2603-12.
[32]. Prast B, Lammers B, Betting M. CFD For Supersonic Gas Processing. In 5th Int Conf on CFD in Process Industries CSIRO, Melbourne, Australia, 2006, pp. 1-6.
[33]. Jiang W, Bian J, Wu A, Gao S, Yin P, Hou D. Investigation of supersonic separation mechanism of CO2 in natural gas applying the Discrete Particle Method. Chem Eng Process 2018;123:272-9.
[34]. Ma Q, Hu D, Jiang J, Qiu Z. A turbulent Eulerian multi-fluid model for homogeneous nucleation of water vapour in transonic flow. Int J Comput Fluid Dynam 2009;23:221-31.
[35]. Shooshtari SR, Shahsavand A. Reliable prediction of condensation rates for purification of natural

gas via supersonic separators. Sep Purif Technol 2013;116:458-70.
[36]. Ding H, Wang C, Wang G. Analytic equations for the Wilson point in high pressure steam flow through a nozzle. Int J Heat Mass Transf 2015;91:961–8.
[37]. Castier M. Modeling and simulation of supersonic gas separations. J Nat Gas Sci Eng 2014;18:304-11.
[38]. Dykas S, Majkut M, Smołka K, Strozik M. Comprehensive investigations into thermal and flow phenomena occurring in the atmospheric air two-phase flow through nozzles. Int J Heat Mass Transf 2017;114:1072-85.
[39]. Dykas S, Majkut M, Smołka K, Strozik M Study of the wet steam flow in the blade tip rotor linear blade cascade. Int J Heat Mass Transf 2018;120:9-17.
[40]. Ma Q, Hu D, He G. Performance of inner-core supersonic gas separation device with droplet enlargement method. Chinese J Chem Eng 2009;17(6):925-33.
[41]. Ding H, Wang C, Chen C. Non-equilibrium condensation of water vapor in sonic nozzle. Appl Therm Eng 2014;71(1):324-34.
[42]. Niknam PH, Mortaheb HR, Mokhtarani B. Dehydration of low-pressure gas using supersonic separation: Experimental investigation and CFD analysis. J Nat Gas Sci Eng 2018;52:202-14.
[43]. Shooshtari SR, Shahsavand A. Optimal operation of refrigeration oriented supersonic separators for natural gas dehydration via heterogeneous condensation. Appl Therm Eng 2018;139:76-86.
[44]. Dykas S, Numerical calculation of the steam condensing flow. Task Q 2001;5:51-35.
[45]. Bian J, Cao X, Yang W, Du H, Yin P. Effects of external particles on the liquefaction property of natural gas in a Laval nozzle. Powder technol 2018;339:894-902.
[46]. Yang Y, Zhu X, Yan Y, Ding H, Wen C. Performance of supersonic steam ejectors considering the nonequilibrium condensation phenomenon for efficient energy utilisation. Appl Energy 2019;242:157-67.
[47]. Mccallum M, Hunt R. The flow of wet steam in a one-dimensional nozzle. Int J Numer methods Eng 1999;44(12):1807-21.
[48]. Marti J, Mauersberger K. A survey and new measurements of ice vapor pressure at temperatures between 170 and 250 K. Geophys Res Lett 1993;20(5):363-6.
[49]. Zhong X, An improved generalized Watson equation for prediction of latent heat of vaporization. Chem Eng Commun 1984;29:257-69.
[50]. O'Rourke PJ. Collective Drop Effects on Vaporizing Liquid Sprays. PhD thesis. Princeton University, Princeton, New Jersey. 1981.
[51]. Dykas S, Wróblewski W. Two-fluid model for prediction of wet steam transonic flow. Int J Heat Mass Transf 2013;60:88-94.
[52]. Ounis H, Ahmadi G, McLaughlin JB. Brownian diffusion of submicrometer particles in the viscous sublayer. J Colloid Interf Sci 1991:143:266-77.
[53]. Wang C, Cao P, Ding H, Wang X, Lin D. Signal analysis of supersonic vapor condensation in nozzle sensor using distributed transient pressure probes. IEEE Trans Instrum Meas 2018;68(4):1053-61.
[54]. Wyslouzil BE, Heath CH. Binary condensation in a supersonic nozzle. J Chem Phys 2000;113(17):

7317-29.
[55]. Wang B, Xu D, Chu K, Yu A. Numerical study of gas–solid flow in a cyclone separator. Appl Math Model, 2006;30(11):1326-42.
[56]. Wood AB. A textbook of sound, G. Bell and Sons Ltd., London, 1930.
[57]. Kieffer, SW. Sound speed in liquid-gas mixtures: Water-air and water-steam. J Geophys Res, 1977;82(20):2895-904.
[58]. Ding H, Li Y, Lakzian E, Wen C, Wang C. Entropy generation and exergy destruction in condensing steam flow through turbine blade with surface roughness. Energ Convers Manage, 2019;196:1089-1104.

List of Figure Captions and Table Titles